nature materials

Article

https://doi.org/10.1038/s41563-026-02727-y

Crystal nucleation and growth in high-entropy alloys revealed by atomic electron tomography

Received: 1 July 2026

Accepted: 30 July 2026

Published online: 25 August 2026

Check for updates

Yakun Yuan[1,2], Saman Moniri[1], Yao Yang[1], Jihan Zhou[1], Andrew Yuan[1], Dennis S. Kim[1], Yongsoo Yang[1], Chenyang Li[3], Kun Luo[4], Qi An[4], Wei Chen[3], Peter Ercius[5] & Jianwei Miao[1]

High-entropy alloys combine multiple principal elements and can exhibit exceptional mechanical properties and catalytic activity. However, how they crystallize remains poorly understood because early nuclei are small, transient and chemically complex. Here we advance atomic electron tomography to determine the three-dimensional atomic structures and local chemical order of 8,160 high- and medium-entropy alloy nuclei. We find that nucleation proceeds through gradient ordering, in which structural order is highest at the core, decreases smoothly towards the boundary and is coupled to local chemical order. Most nuclei coalesce with nearly aligned crystal lattices, whereas a minority form twin boundaries. We develop the gradient nucleation pathways model, which generalizes classical nucleation theory by incorporating spatially varying structural order within each nucleus. The model captures diffuse, partially ordered nuclei, recovers classical nucleation theory in the sharp-interface limit and reveals multiple intermediate states. These results provide an atomistic framework for understanding crystal nucleation and growth across a broad range of materials.

High-entropy alloys (HEAs) arise from a balance between the mixing entropy of multiple principal elements and the formation enthalpy of intermetallic phases, creating a vast multidimensional compositional space for developing structural and functional materials[1–4]. In metallurgy, HEAs can offer an exceptional balance of strength and ductility[4–8], whereas in catalysis, their chemically diverse surfaces provide a nearly continuous range of adsorbate binding energies[9–14]. Understanding nucleation and growth in HEAs is essential for elucidating their formation as well as engineering their properties. However, owing to the lack of direct experimental methods for resolving three-dimensional (3D) local atomic structures, previous studies of HEA nucleation have primarily relied on molecular dynamics (MD) and Monte Carlo simulations, supplemented by indirect experimental measurements[15–19]. Consequently, the atomic mechanisms governing nucleation and growth in HEAs remain elusive.

This knowledge gap reflects a broader challenge in nucleation science. Crystal nucleation underpins phase transformations across physical[20–22], chemical[23–25] and biological systems[26–28]. Classical nucleation theory (CNT) has long served as the standard framework[20–22], but its idealization of a spatially uniform nucleus bounded by a sharp interface is often unrealistic, and its predicted nucleation rates can differ from experimental values by several orders of magnitude[23,29,30]. These limitations have motivated non-classical theories that incorporate diffuse ordering[21,31,32], precursor states[23,33–35] or particle attachment[28,36].

[1]Department of Physics and Astronomy and California NanoSystems Institute, University of California, Los Angeles, CA, USA. [2]Future Material Innovation Center, School of Materials Science and Engineering, Zhangjiang Institute for Advanced Study, and School of Physics and Astronomy, Shanghai Jiao Tong University, Shanghai, China. [3]Department of Materials Design and Innovation, University at Buffalo, The State University of New York, Buffalo, NY, USA. [4]Department of Materials Science and Engineering, Iowa State University, Ames, IA, USA. [5]National Center for Electron Microscopy, Molecular Foundry, Lawrence Berkeley National Laboratory, Berkeley, CA, USA. e-mail: j.miao@ucla.edu

Experimental tests, however, have remained limited by the absence of atom-by-atom measurements of individual nuclei. Here we combine the rapid quenching of HEA and medium-entropy alloy (MEA) nanoparticles[14,37] with atomic electron tomography[38–40] (AET) to kinetically arrest thousands of nuclei spanning a range of nucleation states and reconstruct their 3D atomic structures. This approach enables the quantitative mapping of how local structural and chemical order evolve together during nucleation. The measured structural-order profiles form the basis of gradient nucleation pathways (GNPs), a framework that extends CNT to describe diffuse, partially ordered nuclei.

Structural order in HEA nanoparticles

HEA and MEA nanoparticles were prepared using carbothermal shock synthesis[14,37]. Metal precursors with the desired multielement compositions were loaded onto supports, rapidly heated to ~2,000 K for ~50 ms and then quenched at a characteristic cooling rate of ~10^5 K s^{-1} (Methods). This rapid thermal cycle limited long-range diffusion and preserved, at room temperature, nuclei with different degrees of structural order. Tomographic tilt series were acquired from 25 HEA nanoparticles (HEA1–25; Extended Data Table 1) and 6 NiPdPt MEA nanoparticles using annular dark-field scanning transmission electron microscopy (ADF-STEM). Following image preprocessing, each tilt series was reconstructed using the real-space iterative reconstruction (RESIRE) algorithm[41]. Atomic positions were then traced from the reconstruction and refined to generate a 3D atomic model of each nanoparticle[42] (Methods). The positional precision was estimated to be 21 pm (ref. 43). Figure 1a–c shows three representative HEA atomic structures, namely, HEA2, HEA6 and HEA10, with low, intermediate and high crystallinity, respectively. In the MEA nanoparticles, Ni, Pd and Pt atoms were individually resolved. In the HEA nanoparticles, AET could not reliably distinguish elements with very similar atomic numbers[44]. The eight HEA elements were, therefore, grouped into three experimentally resolvable atomic-number-contrast types: type 1, Co/Ni (blue); type 2, Ru/Rh/Pd/Ag (yellow); and type 3, Ir/Pt (red) (Methods).

For each atom, the local structural order was quantified using a normalized bond-orientational order (BOO) parameter (Methods). The BOO scale is referenced to the face-centered cubic (fcc) order, with BOO = 1 corresponding to a perfect fcc local arrangement and BOO = 0 to a random local arrangement. This normalization is appropriate for the fcc-forming HEA and MEA nanoparticles studied here, and the underlying bond-order descriptors can still distinguish fcc, hexagonal close-packed (hcp), body-centered cubic and disordered local environments (Extended Data Fig. 1). Atoms with BOO ≥ 0.5 were classified as crystalline[43], giving crystallinities of 22.2% to 99.9% across the 25 HEA nanoparticles (Extended Data Fig. 1). Figure 1d–f shows the 3D BOO distributions of HEA2, HEA6 and HEA10, with crystallinities of 26.8%, 55.2% and 86.8%, respectively. In HEA2, ordered regions with BOO ≥ 0.5 are sparse and localized, with only a few regions reaching BOO ≥ 0.7 (Fig. 1d). HEA6 remains heterogeneous but contains a larger fraction of ordered regions with BOO ≥ 0.5 (Fig. 1e). In HEA10, crystalline structural order is more extensive and extends through much of the particle (Fig. 1f).

Complementary structural descriptors support this BOO-based picture. Across the 25 HEA nanoparticles, the pair distribution functions sharpen from broad, amorphous-like correlations in HEA1 to well-defined crystalline peaks in HEA25 (Fig. 1g, from bottom to top). Voronoi tessellation describes the local polyhedron around each atom using the index $<n_3, n_4, n_5, n_6>$, where n_i is the number of faces with i edges, thereby capturing both local topology and coordination[43,45]. Figure 1h shows the 12 most abundant Voronoi polyhedra in HEA2, HEA6 and HEA10. The increased abundance of the ordered local polyhedra <0, 3, 6, 3> and <0, 4, 4, 4> from HEA2 to HEA10 further supports the progression from broadly disordered atomic arrangements to a more crystalline local order.

3D atomic structure of HEA nuclei

HEA nuclei were identified using a BOO-based criterion (Methods). Atoms with BOO ≥ 0.5 were grouped into ordered regions, local BOO maxima defined the nucleus cores and intervening local minima separated the neighbouring nuclei. This procedure identified 7,662 nuclei from 25 HEA nanoparticles spanning a range of arrested nucleation states. Figure 2a–e shows five representative nuclei containing 10, 96, 238, 613 and 1,290 atoms, together with their 3D BOO distributions. The nuclei are non-spherical and internally graded, with structural order concentrated near the core and decreasing towards the boundary, revealing spatially heterogeneous ordering within individual nuclei. Larger nuclei show ordered regions that extend farther from the core (Fig. 2a–e). Across all nuclei, the population decreases exponentially with nucleus size (Fig. 3a), whereas the core BOO increases systematically with nucleus size (Fig. 3b).

To quantify this internal ordering, BOO values were radially averaged for each nucleus. Figure 3c shows the average BOO profiles as a function of radial distance for five nucleus-size classes: 1–10 atoms (blue dots), 11–100 atoms (red dots), 101–500 atoms (yellow dots), 501–1,000 atoms (purple dots) and >1,000 atoms (green dots). All five classes show a smooth decrease in BOO from the core to the boundary. Larger nuclei have higher core BOO values and broader ordered regions, consistent with the strengthening of structural order at the core and the outward expansion of order during growth. The radial profiles were fitted with a generalized Gaussian function, $\alpha(r) = \alpha_0 \times e^{-\left(\frac{r}{R}\right)^{\beta}}$, where α_0, R and β are fitting parameters. The fits are shown as solid curves in Fig. 3c, and the fitted parameters are listed in Extended Data Table 2. These structural trends were robust to a stricter BOO threshold of 0.6 and to the measured positional uncertainty (Extended Data Fig. 2). These features are not fully captured by the idealized assumptions of CNT or by the two-step model. In CNT, a nucleus is represented as a compact, bulk-like crystal with a uniform interior, a sharp interface and a size described primarily by its radius[20–22]. In the two-step model, a dense, disordered cluster forms before the appearance of a crystalline nucleus[23,33–35]. The HEA nuclei observed here are instead diffuse and internally graded: structural order is the highest near its core, decreases smoothly towards the boundary, and both core order and spatial extent of ordering increase with the nucleus size.

Gradient nucleation pathways

To account for these diffuse nuclei with core-to-boundary order gradients, we developed GNP (Methods):

$$\Delta G = -\int \Delta g \alpha(\mathbf{r})\, dV + \int \gamma\, |\nabla \alpha(\mathbf{r})|\, dV, \quad (1)$$

where ΔG is the total free-energy change, Δg is the magnitude of the free-energy decrease per unit volume, $\alpha(\mathbf{r})$ is an order parameter between 0 and 1 and γ is the interfacial tension of the corresponding sharp interface. The first term describes the bulk free-energy gain, weighted by the local degree of structural ordering. The second term describes the interfacial cost of a diffuse nucleus. It is obtained by dividing the nucleus into many small-volume elements and summing the local interfacial contributions associated with spatial changes in $\alpha(\mathbf{r})$ (Extended Data Fig. 3a). Unlike standard squared-gradient diffuse-interface formulations[31,46], GNP uses a lower-order magnitude-gradient interfacial term that is linear in the gradient magnitude with a coefficient equals to the interfacial tension of the corresponding sharp interface (Methods).

Substituting the experimentally fitted radial BOO profiles in Fig. 3c for $\alpha(\mathbf{r})$ in equation (1), we evaluated ΔG. Figure 3d shows that nucleation proceeds through a series of evolving intermediate states, rather than along a single sharp-interface pathway. With increasing

https://doi.org/10.1038/s41563-026-02727-y

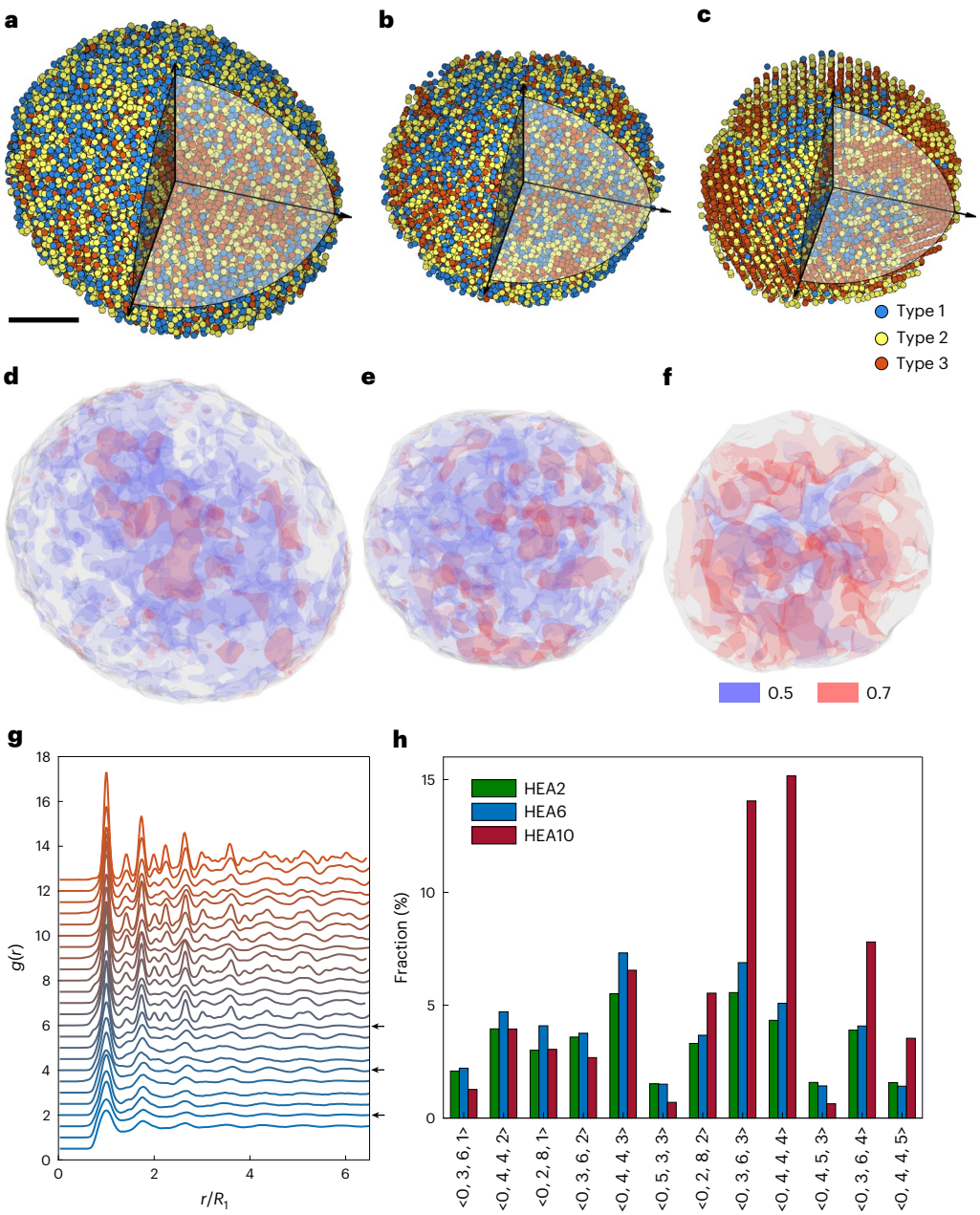

Fig. 1 | 3D atomic structure, chemical type and structural order of HEA nanoparticles spanning a range of crystallinities. a–c, Experimental 3D atomic models of HEA2 (**a**), HEA6 (**b**) and HEA10 (**c**), which represent low, intermediate and high crystallinity, with crystallinities of 26.8%, 55.2% and 86.8%, respectively. Atoms are coloured by experimentally resolved atomic-number-contrast type: type 1, Co/Ni (blue); type 2, Ru/Rh/Pd/Ag (yellow); and type 3, Ir/Pt (red). Crystallinity is defined as the fraction of atoms with normalized BOO ≥ 0.5. **d–f**, 3D isosurfaces of local structural order in the same nanoparticles as in **a–c** at BOO = 0.5 (blue) and BOO = 0.7 (red). **g**, Pair distribution functions of all 25 HEA nanoparticles, ordered from HEA1 (bottom) to HEA25 (top), showing progressively sharper correlations with increasing structural order. Arrows indicate HEA2, HEA6 and HEA10. r/R_1 is the distance (r) normalized by the first peak position (R_1). **h**, Fractions of the 12 most abundant Voronoi polyhedra in HEA2 (green), HEA6 (blue) and HEA10 (red), arranged by increasing coordination number. Scale bar, 2 nm (**a–c**).

nucleus size, the core becomes more crystalline and the ordered region expands outward, producing a sequence of nucleation free-energy barriers that rise with the extent of structural ordering. The analytical profiles in Extended Data Fig. 3b,c illustrate the same principle, showing that a diffuse interface reduces the free-energy barrier relative to the sharp-interface CNT limit. Thus, GNP places CNT and two-step nucleation in a broader framework (Extended Data Fig. 3d–f). CNT is recovered when the order parameter changes abruptly at the interface, producing a single free-energy barrier. The two-step model introduces a metastable precursor and a second barrier. By contrast, the HEA nuclei measured here follow multiple intermediate states in which structural order and the free-energy barrier evolve together.

To test whether gradient ordering persists beyond the type-resolved HEA data, we applied the same GNP analysis to 498 nuclei in six NiPdPt MEA nanoparticles, where Ni, Pd and Pt were resolved atom by atom (Methods). The MEA nuclei show the same trends as the HEA nuclei, with their population decreasing exponentially with size, and their radially averaged BOO profiles decreasing smoothly from core to boundary (Extended Data Fig. 4a,b). Larger MEA nuclei also have a higher core BOO and broader ordered regions, and the profiles

https://doi.org/10.1038/s41563-026-02727-y

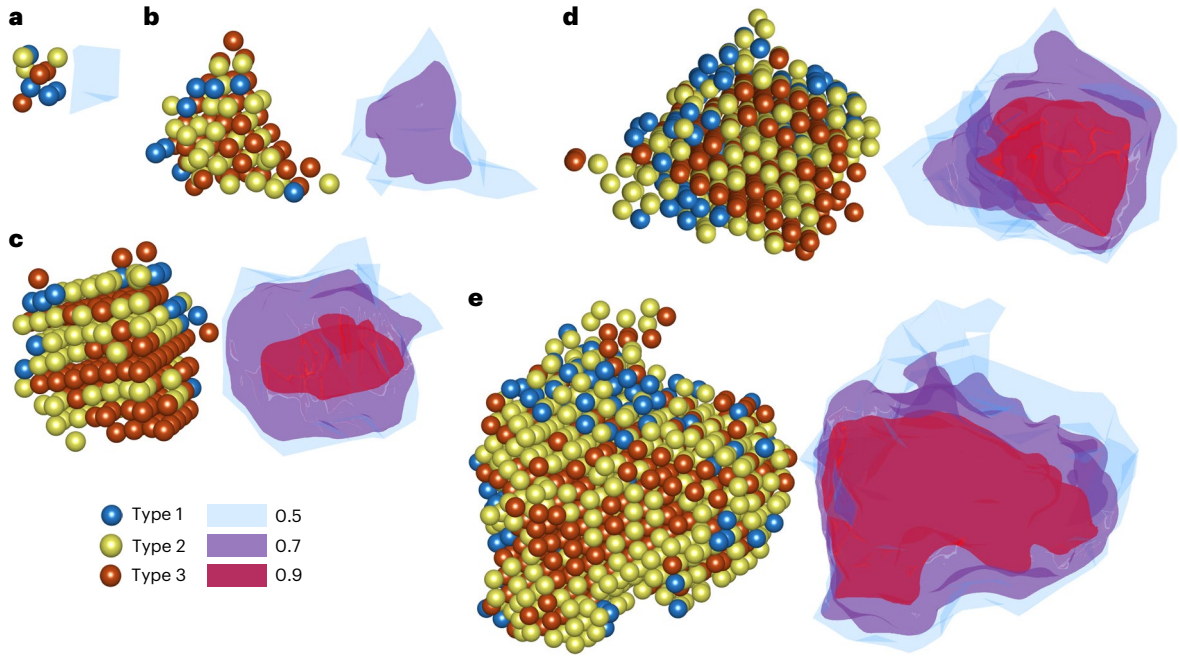

Fig. 2 | 3D structural order of HEA nuclei. a–**e**, Five representative HEA nuclei containing 10 (**a**), 96 (**b**), 238 (**c**), 613 (**d**) and 1,290 (**e**) atoms. Isosurface renderings show BOO values of 0.5 (blue), 0.7 (purple) and 0.9 (red), revealing that structural order is concentrated near the nucleus core and extends outward with increasing nucleus size.

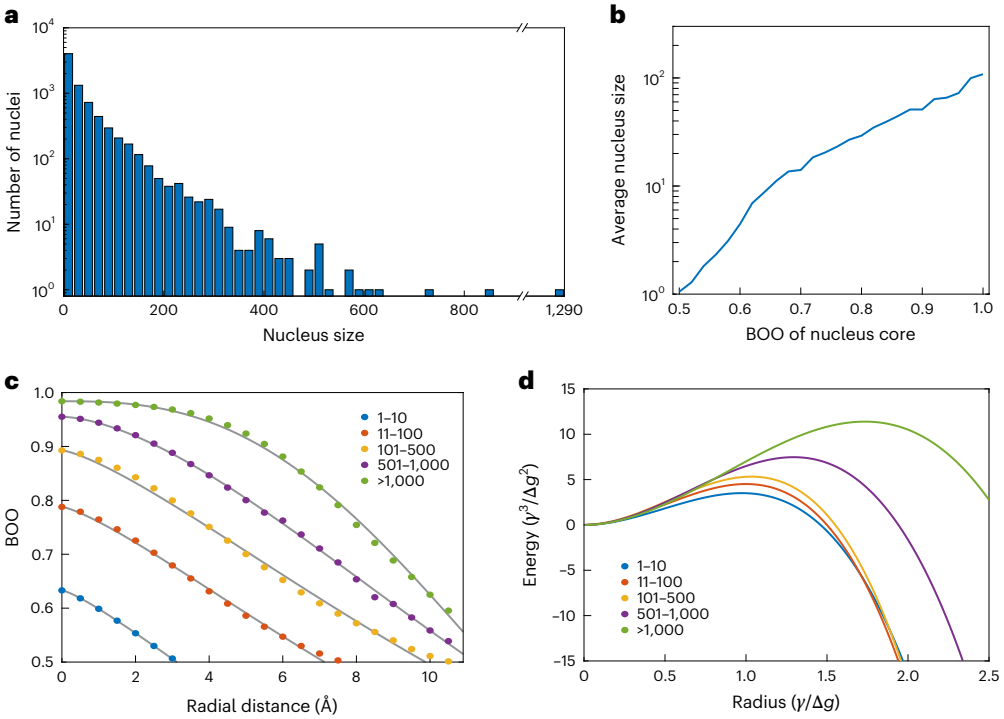

Fig. 3 | Gradient nucleation pathways. a, Number of nuclei as a function of the nucleus size, showing an exponential decrease. **b**, Average nucleus size as a function of BOO at the nucleus core, showing that nuclei with more highly ordered cores are larger. **c**, Average BOO profiles as a function of radial distance for five nucleus-size classes: 1–10 atoms (blue), 11–100 atoms (red), 101–500 atoms (yellow), 501–1,000 atoms (purple) and >1,000 atoms (green). Solid curves are generalized Gaussian fits. **d**, Total free-energy change, ΔG, calculated by substituting the fitted BOO profiles in **c** for $\alpha(\mathbf{r})$ in equation (1), plotted in reduced units as a function of radius. The curves reveal multiple intermediate states with increasing free-energy barriers as structural order strengthens and expands outward.

are well described by generalized Gaussian fits (Extended Data Fig. 4b). Substituting these MEA BOO profiles for $\alpha(\mathbf{r})$ in equation (1) gives ΔG curves that reveal a sequence of intermediate states, with the free-energy barrier increasing as the ordered region expands, consistent with the HEA results (Fig. 3d and Extended Data Fig. 4c).

Ab initio molecular dynamics (AIMD) simulations of an HEA with the same eight elements provided an independent atomistic test during cooling from 2,300 K to 300 K (Methods). We identified 4,591 simulated nuclei, whose size distribution decreases exponentially (Extended Data Fig. 5a). As in the experiments, their radially averaged BOO profiles

https://doi.org/10.1038/s41563-026-02727-y

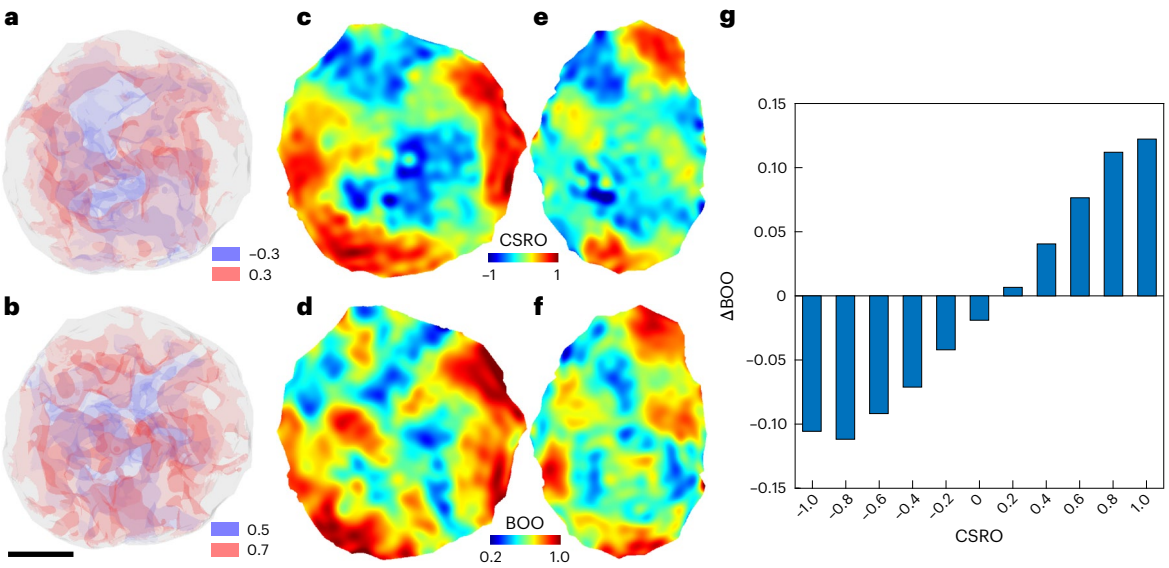

Fig. 4 | Correlation between local chemical and structural order during nucleation. a,**b**, 3D volume renderings of CSRO, α_{33} (**a**) and BOO (**b**) in HEA10, showing spatially heterogeneous chemical and structural order. **c**–**f**, Perpendicular XY (**c**,**d**) and XZ (**e**,**f**) slices through HEA10, showing α_{33} (**c**,**e**) and BOO (**d**,**f**). Type-3-enriched regions spatially coincide with regions of higher structural order. **g**, Change in BOO, ΔBOO, as a function of α_{33}, averaged over the 25 HEA nanoparticles, showing that higher structural order is associated with type-3-enriched local environments. Results for the other CSRO parameters are shown in Extended Data Fig. 7a–c. Scale bar, 2 nm (**a**,**b**).

decrease smoothly from core to boundary and are well described by generalized Gaussian fits (Extended Data Fig. 5b). Applying equation (1) to these simulated BOO profiles gives ΔG curves with increasing free-energy barriers across intermediate states (Extended Data Fig. 5c). Tracking one representative nucleus during continuous cooling from 1,300 K to 700 K further shows outward expansion of the BOO profile and the corresponding evolution of ΔG (Extended Data Fig. 5d,e). To test whether this behaviour is robust across alloy chemistry and cooling protocol, we analysed the MD simulations of NiPt, CoNi, CoPd and CrCoNi under isothermal supercooling and rapid quenching at 1×10^{10} K s^{-1} (Methods). Across all four alloys and both protocols, the BOO profiles show the same core-to-boundary decrease, and larger nuclei have higher core BOO and broader ordered regions (Extended Data Fig. 6). These simulations further support the central finding that nuclei are diffuse and structurally graded, rather than the compact sharp-interface nuclei of CNT[20–22] or the two-step model in which dense disordered precursors form before crystalline nuclei emerge[23,33–35].

Chemical–structural order coupling during nucleation

To determine how local chemistry is coupled to nucleation, we calculated the chemical short-range order (CSRO) parameter, α_{ij}, for each atom from the chemical types of its nearest neighbours[44,47] (Methods). CSRO reports whether a local environment is enriched in one chemical type or mixed between two types: for $i = j$, a positive α_{ii} indicates segregation of type i, whereas for $i \neq j$, a negative α_{ij} indicates intermixing between types i and j. Because the eight HEA elements are resolved as three atomic-number-contrast types, the HEA CSRO results are interpreted at the type level. In HEA10, 3D maps of α_{33} and BOO show that both chemical and structural order are spatially heterogeneous (Fig. 4a,b). Two perpendicular slices show that type-3 (Ir/Pt)-enriched regions overlap with regions of higher BOO (Fig. 4c–f). Across all 25 HEA nanoparticles, ΔBOO, defined as the local BOO minus the mean BOO of the corresponding nanoparticle, increases with α_{33} (Fig. 4g), indicating that nuclei are preferentially associated with type-3-enriched local environments. The remaining CSRO parameters show that structural order is lower in regions with type-1–type-2 intermixing (Extended Data Fig. 7a–c).

Beyond this nucleus-level correlation, particle-to-particle composition also correlates with crystallinity. Across the 25 HEA nanoparticles, crystallinity increases with the type-3 fraction and decreases with the type-1 fraction, whereas type 2 shows no clear trend (Methods). Thus, structural ordering is linked both to the local chemical environment around nuclei and to the overall composition of each nanoparticle. The element-resolved MEA data provide an independent test at a higher chemical resolution, showing that across the six NiPdPt nanoparticles, higher BOO is associated with Pt-enriched regions, whereas lower BOO is associated with Ni-Pd intermixing (Extended Data Fig. 7d–f). These type-resolved HEA and element-resolved MEA data show that nucleation is coupled to the local chemical order, with the favourable chemical environment depending on alloy composition.

To test whether chemistry-structure coupling extends beyond the experimental HEA and MEA systems, we analysed the MD simulations of NiPt, CoNi, CoPd and CrCoNi under two conditions: isothermal nucleation at fixed supercooling and continuous quenching at 1×10^{10} K s^{-1} (Methods). Across all alloys and cooling protocols, the change in BOO varies systematically with CSRO (Extended Data Fig. 8), showing that the local chemical environment and structural ordering are coupled during nucleation. The chemical environments associated with the higher structural order vary by alloy: Ni-rich and reduced Ni-Pt intermixing regions in NiPt, Co-Ni intermixed regions in CoNi, Pd-rich and Co-poor regions in CoPd and Co-rich or Cr-Co intermixed regions in CrCoNi. These alloy-dependent trends show that local chemistry and structural ordering are coupled across compositions, whereas the specific chemical environment associated with higher order depends on the alloy. Combined with the type-resolved HEA data, element-resolved MEA data and synthesis-kinetics analysis, the MD simulations support the interpretation that local chemical environments influence where structural order develops, rather than the CSRO-BOO coupling arising solely from post-nucleation diffusion (Methods).

Nucleus coalescence and twin formation

At later growth stages, neighbouring nuclei can grow into contact and coalesce. To examine their crystallographic relationship before and after contact, we assigned an orientation to each nucleus by template matching and measured the minimum misorientation angle θ between

https://doi.org/10.1038/s41563-026-02727-y

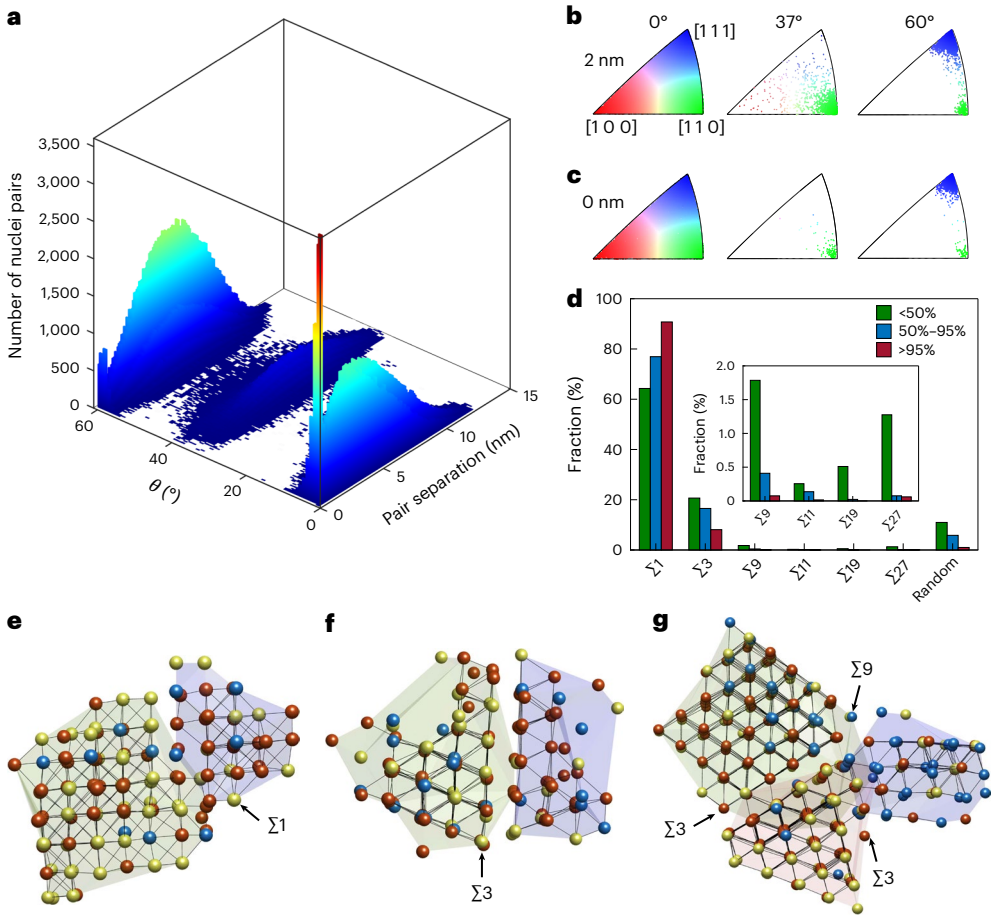

Fig. 5 | Nucleus coalescence and twin formation. a, Distribution of nucleus pairs as a function of minimum misorientation angle θ and pair separation, revealing three groups near 0°, 37° and 60°. **b**,**c**, Stereographic triangles showing the rotation axes of nucleus pairs separated by 2 nm (**b**) and in contact (0 nm; **c**), for the three misorientation groups. Red, green and blue points denote rotation axes near [100], [110] and [111], respectively. **d**, Distributions of CSL Σ boundaries among coalesced nucleus pairs in the 25 HEA nanoparticles, grouped by overall crystallinity: <50% (green), 50%–95% (blue) and >95% (red). The inset enlarges the higher-Σ and random boundary classes. **e**, Representative Σ1 boundary between two nearly aligned coalesced nuclei. **f**, Representative Σ3 boundary corresponding to twin formation. **g**, Three coalesced nuclei forming two Σ3 boundaries and one Σ9 boundary. Atoms in **e**–**g** are coloured by atomic-number-contrast type, as shown in Fig. 1.

nucleus pairs (Methods). The pair distribution in Fig. 5a shows three main misorientation groups near 0°, 37° and 60°. As the pair separation decreases to zero, the 0° group becomes dominant, indicating that most nuclei coalesce with little or no misorientation. A smaller 60° group remains, whereas the 37° group is depleted at contact. Stereographic triangle plots at separations of 2 nm and 0 nm show the corresponding rotation axes (Fig. 5b,c). As expected for nearly aligned nuclei, the 0° group has no preferred rotation axis. At contact, the residual 37° group is concentrated near [110], whereas the 60° group is concentrated mainly near [111], with a smaller contribution near [110]. These results indicate two principal coalescence modes: nearly aligned attachment and a 60° [111] twin-related pathway.

To quantify these coalescence pathways, we classified the crystallographic relationship between contacting nuclei using coincidence-site lattice (CSL) analysis[48,49] (Methods). For each coalesced pair, we calculated the Σ value to quantify lattice coincidence across the boundary, with Σ1 indicating nearly identical orientations and higher Σ values corresponding to lower lattice coincidence. Figure 5d shows the Σ-boundary distributions for the 25 HEA nanoparticles, grouped by overall crystallinity (<50%, 50%–95% and >95%). Σ1 boundaries dominate in all three groups, showing that most nuclei coalesce with little or no misorientation (Fig. 5e). Σ3 boundaries are the second most common and correspond to a 60° rotation about [111] in fcc crystals, consistent with twin formation (Fig. 5f).

In addition to the dominant Σ1 and Σ3 boundaries, Fig. 5d shows small fractions of higher-Σ boundaries, including Σ9, Σ11, Σ19 and Σ27, as well as random boundaries. Among these high-Σ boundaries, Σ9 is the most common and can arise from the intersection of two Σ3 twin boundaries. Figure 5g shows a representative case in which three coalesced nuclei form two Σ3 boundaries and one Σ9 boundary. Across nanoparticles grouped by increasing overall crystallinity, the fraction of Σ1 boundaries rises from 66.1% to 90.8%, whereas the fraction of Σ3 boundaries decreases from 17.8% to 8.1% and the higher-Σ and random boundaries remain minor (Fig. 5d). These results show that nuclei grow primarily through nearly aligned coalescence, with twin formation as a secondary pathway. This atomically resolved picture complements in situ TEM studies of nanocrystal growth and coalescence[49,50].

Conclusion

By resolving 7,662 HEA nuclei and 498 MEA nuclei in three dimensions, atom by atom, we obtained a direct atomic picture of how complex-alloy crystals emerge from disordered nanoparticles. The nuclei are diffuse and exhibit gradient ordering, with structural order highest at the core and decreasing smoothly towards the boundary, whereas the ordered region extends outward as the nuclei grow. Local chemical environments influence where higher order develops. These measured structural-order profiles underpin GNP, which evaluates the nucleation free-energy changes associated with multiple intermediate states and

recovers CNT in the sharp-interface limit. At later stages, neighbouring nuclei grow primarily by nearly aligned coalescence, with twin formation as a secondary pathway. Thus, crystallization in compositionally complex alloys is governed by the coupled evolution of structural order, local chemistry and crystallographic alignment.

These results establish a general strategy for studying crystallization far from equilibrium by arresting transient states, reconstructing their 3D atomic structures and mapping spatial variations in local order. The approach can be extended beyond carbothermal shock synthesis[14,37] and compositionally complex alloys to other phase transformations whose intermediate states can be trapped and structurally resolved[40]. GNP broadens this strategy by using spatial variations in an order parameter to evaluate the free-energy changes of diffuse, partially ordered nuclei. By directly linking the internal structure of individual nuclei to nucleation energetics, the approach enables quantitative tests of how composition and local structural and chemical order influence crystallization pathways. The experimental strategy and GNP, therefore, provide a general framework for understanding nucleation and growth across a wide range of crystallizing systems[20–28].

Online content

Any methods, additional references, Nature Portfolio reporting summaries, source data, extended data, supplementary information, acknowledgements, peer review information; details of author contributions and competing interests; and statements of data and code availability are available at https://doi.org/10.1038/s41563-026-02727-y.

References

1. Yeh, J. W. et al. Nanostructured high-entropy alloys with multiple principal elements: novel alloy design concepts and outcomes. *Adv. Eng. Mater.* **6**, 299–303 (2004).
2. Cantor, B., Chang, I. T. H., Knight, P. & Vincent, A. J. B. Microstructural development in equiatomic multicomponent alloys. *Mater. Sci. Eng. A* **375–377**, 213–218 (2004).
3. Miracle, D. B. & Senkov, O. N. A critical review of high entropy alloys and related concepts. *Acta Mater.* **122**, 448–511 (2017).
4. Zhang, Y. et al. Microstructures and properties of high-entropy alloys. *Prog. Mater Sci.* **61**, 1–93 (2014).
5. George, E. P., Raabe, D. & Ritchie, R. O. High-entropy alloys. *Nat. Rev. Mater.* **4**, 515–534 (2019).
6. Gludovatz, B. et al. A fracture-resistant high-entropy alloy for cryogenic applications. *Science* **345**, 1153–1158 (2014).
7. Li, Z., Pradeep, K. G., Deng, Y., Raabe, D. & Tasan, C. C. Metastable high-entropy dual-phase alloys overcome the strength-ductility trade-off. *Nature* **534**, 227–230 (2016).
8. Ren, J. et al. Strong yet ductile nanolamellar high-entropy alloys by additive manufacturing. *Nature* **608**, 62–68 (2022).
9. Xie, P. et al. Highly efficient decomposition of ammonia using high-entropy alloy catalysts. *Nat. Commun.* **10**, 4011 (2019).
10. Batchelor, T. A. A. et al. High-entropy alloys as a discovery platform for electrocatalysis. *Joule* **3**, 834–845 (2019).
11. Xin, Y. et al. High-entropy alloys as a platform for catalysis: progress, challenges, and opportunities. *ACS Catal.* **10**, 11280–11306 (2020).
12. Löffler, T., Ludwig, A., Rossmeisl, J. & Schuhmann, W. What makes high-entropy alloys exceptional electrocatalysts? *Angew. Chem. Int. Ed.* **60**, 26894–26903 (2021).
13. Sun, Y. & Dai, S. High-entropy materials for catalysis: a new frontier. *Sci. Adv.* **7**, eabg1600 (2021).
14. Yao, Y. et al. High-entropy nanoparticles: synthesis–structure–property relationships and data-driven discovery. *Science* **376**, eabn3103 (2022).
15. Andreoli, A. F. et al. In situ study of non-equilibrium solidification of CoCrFeNi high-entropy alloy and CrFeNi and CoCrNi ternary suballoys. *Acta Mater.* **212**, 116880 (2021).
16. Gao, Y. et al. Growth pattern of homogeneous and heterogeneous nucleation in high-entropy FeNiCrCoCu alloys. *Cryst. Growth Des.* **22**, 2417–2425 (2022).
17. Sharma, A., Deshmukh, S. A., Liaw, P. K. & Balasubramanian, G. Crystallization kinetics in $Al_xCrCoFeNi$ ($0 \le x \le 40$) high-entropy alloys. *Scr. Mater.* **141**, 54–57 (2017).
18. Huang, X. et al. Characterization of nucleation behavior in temperature-induced BCC-to-HCP phase transformation for high-entropy alloy. *Acta Metall. Sin.* **34**, 1546–1556 (2021).
19. Dasari, S., Sharma, A., Gorsse, S., Chesetti, A. & Banerjee, R. Non-classical nucleation of ordered $L1_2$ precipitates in the FCC based $Al_{0.25}CoFeNi$ high entropy alloy. *J. Appl. Phys.* **134**, 015102 (2023).
20. Porter, D. A., Easterling, K. E. & Sherif, M. Y. *Phase Transformations in Metals and Alloys* (CRC Press, 2009).
21. Kelton, K. F. & Greer, A. L. *Nucleation in Condensed Matter: Applications in Materials and Biology* (Pergamon, 2010).
22. Kashchiev, D. *Nucleation: Basic Theory with Applications* (Butterworth-Heinemann, 2000).
23. Vekilov, P. G. Nucleation. *Cryst. Growth Des.* **10**, 5007–5019 (2010).
24. Erdemir, D., Lee, A. Y. & Myerson, A. S. Nucleation of crystals from solution: classical and two-step models. *Acc. Chem. Res.* **42**, 621–629 (2009).
25. Quinson, J. & Jensen, K. M. Ø. From platinum atoms in molecules to colloidal nanoparticles: a review on reduction, nucleation and growth mechanisms. *Adv. Colloid Interface Sci.* **286**, 102300 (2020).
26. De Yoreo, J. J. & Vekilov, P. G. Principles of crystal nucleation and growth. *Rev. Mineral. Geochem.* **54**, 57–93 (2003).
27. Weiner, S. & Addadi, L. Crystallization pathways in biomineralization. *Annu. Rev. Mater. Res.* **41**, 21–40 (2011).
28. De Yoreo, J. J. et al. Crystallization by particle attachment in synthetic, biogenic, and geologic environments. *Science* **349**, aaa6760 (2015).
29. Sear, R. P. Nucleation: theory and applications to protein solutions and colloidal suspensions. *J. Phys. Condens. Matter* **19**, 033101 (2007).
30. Sosso, G. C. et al. Crystal nucleation in liquids: open questions and future challenges. *Chem. Rev.* **116**, 7078–7116 (2016).
31. Cahn, J. W. & Hilliard, J. E. Free energy of a nonuniform system. I. Interfacial free energy. *J. Chem. Phys.* **28**, 258–267 (1958).
32. Oxtoby, D. W. & Evans, R. Nonclassical nucleation theory for the gas–liquid transition. *J. Chem. Phys.* **89**, 7521–7530 (1988).
33. ten Wolde, P. R. & Frenkel, D. Enhancement of protein crystal nucleation by critical density fluctuations. *Science* **277**, 1975–1978 (1997).
34. Gebauer, D., Völkel, A. & Cölfen, H. Stable prenucleation calcium carbonate clusters. *Science* **322**, 1819–1822 (2008).
35. Vekilov, P. G. The two-step mechanism of nucleation of crystals in solution. *Nanoscale* **2**, 2346–2357 (2010).
36. Penn, R. L. & Banfield, J. F. Imperfect oriented attachment: dislocation generation in defect-free nanocrystals. *Science* **281**, 969–971 (1998).
37. Yao, Y. et al. Carbothermal shock synthesis of high-entropy-alloy nanoparticles. *Science* **359**, 1489–1494 (2018).
38. Miao, J., Ercius, P. & Billinge, S. J. L. Atomic electron tomography: 3D structures without crystals. *Science* **353**, aaf2157 (2016).
39. Miao, J. Computational microscopy with coherent diffractive imaging and ptychography. *Nature* **637**, 281–295 (2025).
40. Zhou, J. et al. Observing crystal nucleation in four dimensions using atomic electron tomography. *Nature* **570**, 500–503 (2019).
41. Pham, M., Yuan, Y., Rana, A., Osher, S. & Miao, J. Accurate real space iterative reconstruction (RESIRE) algorithm for tomography. *Sci. Rep.* **13**, 5624 (2023).
42. Liao, Y. et al. Accurate determination of the 3D atomic structure of amorphous materials. *Nature* **649**, 1123–1129 (2026).

43. Yang, Y. et al. Determining the three-dimensional atomic structure of an amorphous solid. *Nature* **592**, 60–64 (2021).
44. Moniri, S. et al. Three-dimensional atomic structure and local chemical order of medium- and high-entropy nanoalloys. *Nature* **624**, 564–569 (2023).
45. Finney, J. L. Random packings and structure of simple liquids. I. Geometry of random close packing. *Proc. R. Soc. Lond. A* **319**, 479–493 (1970).
46. Boettinger, W. J., Warren, J. A., Beckermann, C. & Karma, A. Phase-field simulation of solidification. *Annu. Rev. Mater. Res.* **32**, 163–194 (2002).
47. Li, Q. J., Sheng, H. & Ma, E. Strengthening in multi-principal element alloys with local-chemical-order roughened dislocation pathways. *Nat. Commun.* **10**, 3563 (2019).
48. Grimmer, H., Bollmann, W. & Warrington, D. H. Coincidence-site lattices and complete pattern-shift in cubic crystals. *Acta Crystallogr.* **A30**, 197–207 (1974).
49. Song, M. et al. Oriented attachment induces fivefold twins by forming and decomposing high-energy grain boundaries. *Science* **367**, 40–45 (2020).
50. Li, D. et al. Direction-specific interactions control crystal growth by oriented attachment. *Science* **336**, 1014–1018 (2012).

Methods

HEA and MEA nanoparticle synthesis and preparation

Two separate carbothermal shock sample sets were prepared: an eight-element HEA set containing Co, Ni, Ru, Rh, Pd, Ag, Ir and Pt, and a three-element MEA set containing Ni, Pd and Pt. Metal precursors were dissolved in ethanol (0.05 M) at the target stoichiometries, dispersed onto reduced graphene oxide substrates and dried in air[14,37]. The supported precursors were Joule heated to ~2,000 K for ~50 ms and then quenched at a characteristic cooling rate of ~10^5 K s^{-1}. This rapid thermal cycle limits long-range diffusion, solute partitioning and coarsening, although it does not eliminate short-range atomic motion during the liquid and supercooled-liquid stages.

AET was performed on 25 HEA nanoparticles from the eight-element sample set and six NiPdPt MEA nanoparticles from the three-element sample set. Although carbothermal shock typically yields highly crystalline solid-solution nanoparticles[14,37], the rapid-quench conditions used here also preserved nanoparticles with varying crystallinity, including particles containing partially ordered regions and incipient nuclei. Each reconstructed nanoparticle can contain multiple nuclei with different sizes and degrees of structural order. Because nucleation is stochastic in space and time, the recovered ensemble spans a range of arrested nucleation and growth states. These data represent frozen ensemble snapshots, not time-resolved observations of the same nanoparticle. We did not classify individual nuclei as subcritical or supercritical, because the critical size depends on the local composition, undercooling and interfacial energy. This ensemble enabled a direct 3D atom-by-atom visualization of arrested nucleation states by AET at room temperature.

AET data acquisition

The experimental AET tilt series of 25 HEA and 6 MEA nanoparticles were acquired using the TEAM 0.5 and TEAM I microscope and TEAM stage at the National Center for Electron Microscopy. The aberration-corrected microscope operated in the ADF mode at an accelerating voltage of 200 or 300 kV (Extended Data Table 1). For each nanoparticle, sample features in its vicinity were identified at each tilt angle to aid in nanoparticle localization and optimize the imaging conditions, thereby minimizing unnecessary exposure to the electron beam. To correct for drift distortion, three to four consecutive images were acquired using the same fast scanning direction and a dwell time of 3 µs. To minimize electron damage, the beam current was optimized, resulting in a total electron dose of 3.4–10.2 × 10^5 e^- $Å^{-2}$ for each tilt series (Extended Data Table 1). Images captured before, during and after the acquisition of each tilt series confirmed that the structural changes of each nanoparticle remained minimal throughout the data collection process.

Image preprocessing

The AET tilt series underwent a detailed multistep preprocessing protocol before tomographic reconstruction, outlined as follows.

(1) Drift correction. Multiple images taken consecutively at each tilt angle were used to determine the drift vector using cross-correlation algorithms. A shift step size of 0.1 pixel was used during the calculation to detect subpixel drift in the images. Using the drift vectors, a two-dimensional mesh grid with corrected pixel positions for each image was computed. The raw images were then interpolated onto the drift-corrected two-dimensional mesh grids and averaged to produce a single drift-corrected image at each angle.

(2) Image denoising. A block-matching and 3D filtering algorithm was used to remove Poisson and Gaussian noise from the drift-corrected images[51]. To optimize the block-matching and 3D filtering algorithm parameters, we first estimated the Poisson and Gaussian noise levels in the experimental images. Subsequently, the same noise levels were added to simulate the ADF-STEM images of a nanoparticle with a similar size and composition to the experimental samples. The optimum parameters were identified by achieving the best cross-correlation between the noise-free images and their denoised versions. Once optimized, these parameters were applied to the experimental images for effective noise reduction.

(3) Background subtraction. To perform background subtraction on the denoised images, a mask slightly larger than the nanoparticle boundary was generated for each image using the Otsu thresholding method. The background beneath the nanoparticle was then estimated using Laplacian interpolation from the boundary of the mask. This estimated background was subsequently subtracted from the denoised image[43].

(4) Image alignment. To align the images in each tilt series about a common tilt axis, the centre-of-mass positions were computed for each image. Each individual image was then shifted so that its centre of mass coincided with the centre of the image. This procedure ensured that all images in the tilt series were properly aligned and ready for AET reconstruction[42,52,53].

AET reconstructions

After preprocessing, each tilt series was reconstructed using the real space iterative reconstruction[41] algorithm with an oversampling ratio of 4. Convergence was achieved over 200 iterations to ensure accuracy. To compensate for nominal tilt angle errors and minor misalignments, an iterative process for angular refinement and spatial alignment was used[41,42]. Following the initial 3D reconstruction, a finer mask of each HEA nanoparticle was projected at each tilt angle, which was used to update the background subtraction and the preprocessed tilt series. The final 3D reconstruction was then obtained using the real space iterative reconstruction algorithm with further angular refinement and spatial alignment.

3D atomic structure and chemical classification

The 3D atomic structure and chemical composition of the HEA and MEA nanoparticles were obtained by tracing atom positions and classifying atom species using the final reconstructions.

i. To trace the 3D coordinates of the atoms, each reconstruction was oversampled by a factor of 3 using spline interpolation. Local maxima were then identified and fitted using a polynomial function within a 0.8 Å × 0.8 Å × 0.8 Å volume, generating a preliminary list of potential atoms[43,54]. Considering the typical atomic radii in HEA and MEAs, a minimum distance of 2 Å between neighbouring atoms was enforced to help rule out unphysical atom locations. Non-atoms, typically originating from weak noise in the reconstruction, were removed by *k*-means clustering of the integrated intensities around potential atoms[55,56]. The remaining atoms were manually checked against the reconstruction slice by slice to correct for misidentified or unidentified atoms, which typically constituted a small fraction (<1%) of the total atom population in each HEA or MEA nanoparticle.

ii. Using the traced atom positions, species classification within each HEA or MEA nanoparticle was conducted in two stages. First, *k*-means clustering was applied to the integrated intensity over a volume of 0.8 × 0.8 × 0.8 $Å^3$ around each atom, resulting in an initial classification into three types for the HEA nanoparticles (Co, Ni as type 1; Ru, Rh, Pd, Ag as type 2; Ir, Pt as type 3) and three individual elements for the MEA nanoparticles (Ni, Pd and Pt). This initial classification was followed by a local classification, where the averaged intensities of type 1–3 atoms within a 10-Å radius around a centre atom were computed[43,44]. The type of each centre atom was then determined by the minimum

L2-norm between its intensity and the averaged intensities of the three types. After iterating through all atoms, the final classification of the three types was obtained.

iii. By fitting each atom type with a Gaussian function, the 3D coordinates of the atoms were further refined by minimizing the L_2-norm error between the calculated and experimental images using a gradient descent algorithm[56]. The final atomic structures of the HEA and MEA nanoparticles with refined 3D coordinates and species were used for further analysis. To ensure the accuracy of subsequent analysis on the atomic structures, surface atoms of each HEA or MEA nanoparticle were excluded before computing the structural and chemical order.

BOO, crystallinity and structural descriptors

The atomic-scale structural order during nucleation was quantified using normalized BOO, based on the averaged local BOO parameters, Q_4 and Q_6 (refs. 57,58). The normalized BOO is defined as $\frac{\sqrt{Q_4^2+Q_6^2}}{\sqrt{Q_{4,\mathrm{fcc}}^2+Q_{6,\mathrm{fcc}}^2}}$, where $Q_{4,\mathrm{fcc}}$ and $Q_{6,\mathrm{fcc}}$ are the corresponding reference values for the fcc lattice. A BOO value of 1 indicates a perfect local fcc arrangement around the corresponding atom, whereas 0 indicates a random arrangement. A BOO cut-off of 0.5 was chosen as the threshold for separating crystalline and amorphous atoms. The crystallinity of each HEA or MEA nanoparticle was defined as the fraction of its constituent crystalline atoms.

In our analysis, only 0.8% of atoms show local hcp order, and 98.7% of these atoms lie along Σ3 twin boundaries between adjacent fcc domains. We observed no contiguous hcp-ordered regions consistent with independent hcp nuclei within our detection limits. This pattern is consistent with the late-transition-metal HEA and MEAs studied here, which stabilize fcc solid solutions at room temperature, and with the propensity for twinning during rapid quenching, where local hcp stacking arises at twin planes rather than as a distinct phase. AIMD simulations capturing the process of crystal nucleation in HEAs during cooling from 2,300 K to 300 K yield an fcc-dominated solidification pathway without stable hcp nuclei (Extended Data Fig. 5), supporting this interpretation.

Identification of nuclei and radial BOO analysis

HEA and MEA nuclei were identified within nanoparticles whose alloy class was determined from synthesis and particle-level composition. For each atom, we defined a spherical neighbourhood with a radius equal to the nearest-neighbour distance, determined from the first minimum in the nanoparticle pair distribution function. If no atom within this neighbourhood had a higher BOO than the considered atom, the atom was treated as a local BOO maximum and used to seed a BOO-defined region. If one or more neighbouring atoms had higher BOO, the considered atom was assigned to the region associated with the neighbouring atom having the highest BOO. This procedure was iterated until all atoms were linked to the local BOO maxima. Connected regions composed of atoms with BOO ≥ 0.5 were identified as nuclei. Because no minimum size was imposed, the smallest detected nuclei consisted of a single ordered core atom surrounded by atoms with BOO < 0.5. For the radial BOO analysis, BOO values were averaged as a function of distance from the geometric centre of each nucleus, given that 73.5% of the nuclei had a BOO-defined core separated from the centre by less than the nearest-neighbour distance of 3.68 Å.

Derivation and scope of GNP

To derive GNP, we assign each atom, molecule or volume element in a nucleus an order parameter $\alpha(\mathbf{r})$, where $\alpha = 0$ represents the parent disordered phase and $\alpha = 1$represents the fully ordered product phase. In this work, $\alpha(\mathbf{r})$ is provided by the measured or MD-simulated BOO profile, but the framework can use any order parameter that tracks the transformation from the parent phase to the product phase. A volume element ΔV with order parameter α contributes $-\Delta g \Delta V \alpha$ to the free energy. Taking the continuum limit gives the first term in equation (1).

To derive the second term in equation (1), we divide the nucleus into many small volumes, each with area Δs and thickness Δd (Extended Data Fig. 3a). Within each element, the order-parameter gradient is taken normal to the area Δs with magnitude $|\Delta\alpha|/\Delta d$, where $\Delta\alpha$ is the change in order parameter across the thickness Δd. The effective interfacial tension associated with this element is calculated as

$$\gamma_{eff} = \frac{|\Delta\alpha|/\Delta d}{1/\Delta d}\gamma = |\Delta\alpha|\gamma \tag{2}$$

where γ denotes the interfacial tension of the corresponding sharp interface and may depend on interface orientation. The total interfacial energy of the nucleus is obtained by summing the contributions from all volume elements:

$$\int |\Delta\alpha|\gamma \mathrm{d}s = \int \gamma \left|\frac{\Delta\alpha}{\Delta d}\right| \mathrm{d}V = \int \gamma |\nabla\alpha| \mathrm{d}V \tag{3}$$

which corresponds to the second term in equation (1). For heterogeneous nucleation, equation (1) can be multiplied by the usual shape factor[20–22].

GNP uses spatially varying order parameters to describe a diffuse nucleus. It differs from conventional squared-gradient formulations, including the Cahn–Hilliard free-energy functional[31] and standard phase-field models[46], which combine a local free-energy density with an interfacial penalty of the form $K|\nabla\phi|^2$. Here ϕ denotes a continuous field, such as composition, density, phase identity or structural order. These approaches are powerful for predicting equilibrium interface profiles and widths, and, when kinetic equations are specified, interface dynamics. GNP addresses a different problem: once a 3D order-parameter profile is specified—whether from experiment, simulation or theory—it evaluates the free-energy change of a nucleus whose internal order may be diffuse and still evolving. Its distinct feature is the magnitude-gradient interfacial term, $\gamma|\nabla\alpha|$, which is linear, or first order, in the gradient magnitude. By contrast, $K|\nabla\phi|^2$ is quadratic, or second order, in the gradient magnitude. The coefficient γ in GNP is the corresponding sharp-interface tension, giving a direct connection to CNT. In squared-gradient theories, K is a gradient-energy coefficient, and the sharp-interface tension is obtained after specifying the local free-energy density and solving, or asymptotically matching, a finite-width interface profile. A Heaviside step profile gives a formally singular energy in $K|\nabla\phi|^2$, whereas in GNP, it gives a finite surface term, γA, and therefore recovers CNT in the sharp-interface limit.

Nucleation free-energy barriers in GNP

To illustrate the energetics of GNP, we evaluated equation (1) for one sharp-interface profile and three diffuse radial profiles. The order parameter $\alpha(\mathbf{r})$ in equation (1) is fully 3D and does not require radial symmetry. The radial profiles below are used only to provide analytical insight and to compare GNP with the CNT limit.

1. Sharp interface. A sharp interface is represented by a Heaviside step function (Extended Data Fig. 3b, black curve):

$$\alpha = \begin{cases} \alpha_0 & r \le R \\ 0 & r > R \end{cases} \tag{4}$$

where $\alpha_0 \le 1$ is the core value of the order parameter. Substituting equation (4) into equation (1) gives

$$\Delta G = -\frac{4\pi}{3}\alpha_0 R^3 \Delta g + 4\pi\alpha_0 R^2 \gamma \tag{5}$$

For $\alpha_0 = 1$, equation (5) reduces to CNT. Differentiating ΔG with respect to R gives

$$r_c^* = \frac{2\gamma}{\Delta g}\Delta G^* \simeq \frac{16.8\gamma^3}{\Delta g^2} \quad (6)$$

As an order-of-magnitude CNT reference, we estimate $\Delta g \approx (\Delta H \Delta T)/(T_m V_m)$, where ΔH is the molar latent heat of melting, $\Delta T = T_m - T$ is the undercooling, T_m is the melting temperature and V_m is the molar volume. Using representative late-transition-metal values, $\gamma \approx 0.2$ J m^{-2}, $\Delta H \approx 15$ kJ mol^{-1}, $T_m \approx 1{,}800$ K, $\Delta T \sim 300$–800 K and $V_m \approx 9$ cm^{3}mol^{-1} gives $r_c^* \sim 0.5$–1.5 nm, corresponding roughly to tens to several hundreds of atoms. Thus, the nuclei analysed here, from single-atom cores to more than 1,000 atoms, span the expected sub-critical, near-critical and post-critical size range.

2. Diffuse interface with a linear decrease. A linear profile is written as

$$\alpha = \alpha_0\left(1 - \frac{r}{R}\right) \quad (7)$$

Substituting equation (7) into equation (1) and maximizing ΔG with respect to R gives

$$r_c^* = \frac{8}{3}\frac{\gamma}{\Delta g}\Delta G^* \simeq \frac{9.9\alpha_0\gamma^3}{\Delta g^2} \quad (8)$$

3. Diffuse interface with a parabolic decrease above the linear profile. This profile is

$$\alpha = \alpha_0\left[1 - \left(\frac{r}{R}\right)^2\right] \quad (9)$$

Substituting it into equation (1) gives

$$r_c^* = \frac{5\gamma}{2\Delta g}\Delta G^* \simeq \frac{13.1\alpha_0\gamma^3}{\Delta g^2} \quad (10)$$

4. Diffuse interface with a parabolic decrease below the linear profile. This profile is

$$\alpha = \alpha_0\left(1 - \frac{r}{R}\right)^2 \quad (11)$$

Substitution into equation (1) gives

$$r_c^* = \frac{10\gamma}{3\Delta g}\Delta G^* \simeq \frac{7.8\alpha_0\gamma^3}{\Delta g^2} \quad (12)$$

Extended Data Fig. 3c shows the corresponding ΔG curves for the profiles in Extended Data Fig. 3b. For the same Δg, γ and α_0, the barrier increases from the most diffuse parabolic profile to the linear profile, the upper parabolic profile and the sharp-interface limit. Thus, diffuse ordering lowers the free-energy barrier relative to the sharp-interface CNT limit, whereas CNT is recovered when the order parameter changes abruptly at the interface.

AIMD simulations

AIMD simulations were performed to follow solidification in an equimolar eight-element HEA using density functional theory in the Vienna ab initio simulation package[59–61]. Exchange and correlation were treated with the PBE generalized-gradient approximation[62], and the Brillouin zone was sampled at the Γ point. The periodic simulation cell contained 400 atoms in a 5 × 5 × 4 fcc conventional-cell box, with Co, Ni, Ru, Rh, Pd, Ag, Ir and Pt randomly assigned in equal fractions. The initial structure was relaxed by conjugate-gradient minimization until forces were below 0.01 eV Å^{-1}. AIMD was carried out in the *NVT* ensemble using a Nosé–Hoover thermostat and a 2-fs time step[63,64]. To generate a liquid-like starting configuration, the system was heated and equilibrated at 2,300 K for 4 ps, and then cooled to 300 K at 1 K ps^{-1}. To improve the computational efficiency, the cooling path was divided into 100-K temperature intervals that were simulated in parallel. This segmented protocol was used to capture the main structural changes during solidification within accessible AIMD timescales. The segmented simulations identified the main nucleation window between 1,300 K and 700 K. To follow nucleus evolution in this range more directly, we performed an additional continuous-cooling AIMD simulation from 1,300 K to 700 K using the same *NVT* settings. This continuous run used a higher cooling rate for computational efficiency and was used to track the qualitative evolution of BOO profiles and the corresponding GNP free-energy curves.

MD simulations of multiple alloy systems

MD simulations were performed with LAMMPS[65] to test whether gradient ordering persists across alloy chemistry and cooling protocol. Interatomic potentials were screened from OpenKIM and the NIST Interatomic Potentials Repository, and potentials producing liquid instabilities or unphysical phase changes were excluded. Production simulations used second-nearest-neighbour MEAM potentials for NiPt[66] and CoPd[67], and EAM/Finnis-Sinclair potentials for CoNi and CrCoNi[68]. Equiatomic random solid solutions were initialized on fcc lattices with periodic boundary conditions. The NiPt, CoNi and CoPd cells contained 108,000 atoms, corresponding to a cubic box of about 11 nm on each side. For CrCoNi, a smaller 6,912-atom cell, about 4.2 nm on each side, was used to obtain fcc solidification within accessible simulation times, and three independent trajectories were run to improve statistics.

The systems were first equilibrated at 3,000 K for 1 ns in the *NVT* ensemble with a Nosé–Hoover thermostat, cooled to 2,000 K over 0.4 ns in the *NPT* ensemble at 0 bar, and then held for another 0.4 ns to obtain a homogeneous disordered state. Crystallization was then simulated using two protocols. In the rapid-cooling protocol, the liquid was continuously quenched from 2,000 K at about 1×10^{10} K s^{-1} in *NPT* at 0 bar. The nucleation temperature, T_n, was identified from the first sharp decrease in potential energy and the corresponding increase in fcc fraction. In the isothermal protocol, configurations taken just above T_n were brought to T_n − 20 K and held in *NPT* at 0 bar to follow spontaneous nucleation and growth. All simulations used a 2-fs time step. Structural evolution was analysed in OVITO using polyhedral template matching with an root-mean-square-deviation cut-off of 0.1 to identify fcc and hcp local motifs[69,70], together with potential-energy monitoring to track the amorphous-to-crystalline transition. BOO and CSRO profiles of NiPt, CoNi, CoPd and CrCoNi nuclei were computed using the same procedures applied to the experimental data (Extended Data Figs. 6 and 8).

CSRO analysis

In our AET experiments, ADF-STEM images were acquired for each nanoparticle, followed by the reconstruction of the 3D atomic structure. The integrated ADF intensity increases strongly with the atomic number. For the MEA nanoparticles, we successfully identified the atomic species as Ni, Pd and Pt. However, for the HEA nanoparticles, the eight constituent elements were classified into three groups due to minimal differences in their atomic numbers: Co and Ni as type 1; Ru, Rh, Pd and Ag as type 2; and Ir and Pt as type 3. The CSRO (α_{ij}) of each atom was computed by analysing the chemical species of its nearest-neighbour atoms using the following equation[44,47,71]:

$$\alpha_{ij} = \frac{p_{ij} - C_j}{\delta_{ij} - C_j} \quad (13)$$

where p_{ij} denotes the probability of finding a j-type atom among the nearest neighbours of an i-type atom, C_j represents the concentration of j-type atoms in the nanoparticle and δ_{ij} is the Kronecker delta function.

Particle-level composition and crystallinity analysis

The overall composition of each HEA nanoparticle was quantified directly from the final classified AET atomic model (Extended Data Table 1). Each atom was assigned to one of three experimentally resolved atomic-number-contrast types: type 1 (Co/Ni), type 2 (Ru/Rh/Pd/Ag) or type 3 (Ir/Pt). Across the 25 HEA nanoparticles, the average compositions were 29.7 ± 8.4% of type 1, 40.1 ± 3.7% of type 2 and 30.2 ± 7.5% of type 3. To test whether particle-level composition correlates with crystallinity, we compared the crystallinity of each HEA nanoparticle with its type fractions. Crystallinity was defined as the fraction of atoms with normalized BOO ≥ 0.5. Pearson correlation coefficients were calculated using one data point per nanoparticle, with two-sided P values for the null hypothesis of zero correlation. Crystallinity was positively correlated with the type-3 fraction ($r = 0.60$, $P = 1.7 \times 10^{-3}$) and negatively correlated with the type-1 fraction ($r = -0.51$, $P = 1.0 \times 10^{-2}$), whereas the type-2 fraction showed no statistically significant correlation ($r = -0.07$, $P = 0.73$).

Synthesis kinetics and MD diffusion analysis

To assess whether the observed CSRO-BOO coupling could arise solely from post-nucleation diffusion, we combined the synthesis–kinetics considerations with MD diffusion analysis. In the carbothermal shock experiments, nanoparticles were heated to ~2,000 K for ~50 ms and quenched at a characteristic cooling rate of ~10^5 K s^{-1}. This rapid thermal cycle limits long-range diffusion, solute partitioning and coarsening, but allows short-range atomic motion during the liquid and supercooled-liquid stages. Atomic mobility was analysed from MD trajectories of NiPt, CoNi and CrCoNi. The crystallization point was identified from the sharp decrease in potential energy and the growth of the fcc fraction. Using unwrapped atomic coordinates, we calculated the mean stepwise displacement over $\Delta t = 4$ ps and the cumulative displacement from the initial configuration for each element. Before crystallization, atoms showed stepwise displacements of ~0.9–1.5 Å every 4 ps and cumulative displacements of ~10–15 Å. After crystallization, the stepwise displacement decreased to ~0.4 Å every 4 ps, and the cumulative displacement became nearly constant. These results indicate that local chemical environments can form before or during early nucleation, whereas substantial chemical rearrangement is strongly suppressed once crystalline order develops. Thus, the data support the interpretation that local chemical environments influence where higher structural order emerges, although limited short-range relaxation during early growth may further sharpen local chemical and structural order.

Nucleus orientation and CSL analysis

The orientation of each nucleus was determined by fitting the 3D coordinates of its atoms to an fcc reference lattice using a brute-force template-matching approach. For each trial orientation, atoms were assigned to the fcc template if their distance from the nearest template site was less than 15% of the fcc lattice parameter. The orientation with the best template match was assigned to the nucleus. Very small nuclei can have ambiguous orientations because they contain too few atoms to define a stable lattice frame. Therefore, only nuclei with at least 13 atoms matched to the fcc template were considered to have well-defined orientations and were used in the orientation analysis.

The orientation of each nucleus was represented by a matrix containing the three lattice vectors of its best-matched fcc template. For each nucleus pair, the relative rotation matrix was calculated from the two orientation matrices and converted to a rotation angle θ and a unit rotation axis $\hat{u}$. Because fcc crystals have cubic symmetry, symmetry-equivalent choices of the template axes can give multiple equivalent values of $(\theta, \hat{u})$ for the same pair. To remove this ambiguity, all symmetry-equivalent choices were tested, and the solution with the smallest rotation angle was selected. This angle is reported as the minimum misorientation angle between the two nuclei.

CSL theory was used to classify the crystallographic relationships between coalesced nucleus pairs[48]. In CSL notation, a boundary is labelled Σn, where n is the ratio between the CSL unit-cell volume and the original crystal unit-cell volume. Smaller n indicates a higher density of coincident lattice sites and stronger lattice matching across the boundary. Reference misorientation angles and unit rotation axes $(\theta_n, \hat{u}_n)$ for each Σn boundary were taken from the literature[48]. Each experimental boundary was classified by comparing its measured minimum misorientation $(\theta, \hat{u})$ with these reference values. A boundary was assigned to Σn when the angular separation between $\hat{u}$ and $\hat{u}_n$ was less than 5° and the misorientation-angle difference satisfied $|\theta - \theta_n| \leq \theta_m$, where $\theta_m = 15°/\sqrt{n}$ follows the Brandon criterion[72]. Boundaries that did not satisfy these criteria were classified as random.

Data availability

Raw and processed experimental data, reconstructed atomic models and analysis data are available via GitHub at https://github.com/AET-HEA-Nucleation/Supplementary-Data-Codes.

Code availability

The MATLAB source code for the 3D reconstruction, atom tracing and data analysis for this paper is available via GitHub at https://github.com/AET-HEA-Nucleation/Supplementary-Data-Codes. The code was developed and tested with MATLAB R2023b (https://matlab.mathworks.com/).

References

51. Dabov, K., Foi, A., Katkovnik, V. & Egiazarian, K. Image denoising by sparse 3-D transform-domain collaborative filtering. *IEEE Trans. Image Process.* **16**, 2080–2095 (2007).
52. Scott, M. C. et al. Electron tomography at 2.4-ångström resolution. *Nature* **483**, 444–447 (2012).
53. Chen, C. C. et al. Three-dimensional imaging of dislocations in a nanoparticle at atomic resolution. *Nature* **496**, 74–77 (2013).
54. Yuan, Y. et al. Three-dimensional atomic packing in amorphous solids with liquid-like structure. *Nat. Mater.* **21**, 95–102 (2022).
55. Lloyd, S. Least squares quantization in PCM. *IEEE Trans. Inf. Theory* **28**, 129–137 (1982).
56. Yang, Y. et al. Deciphering chemical order/disorder and material properties at the single-atom level. *Nature* **542**, 75–79 (2017).
57. Steinhardt, P. J., Nelson, D. R. & Ronchetti, M. Bond-orientational order in liquids and glasses. *Phys. Rev. B* **28**, 784–805 (1983).
58. Lechner, W. & Dellago, C. Accurate determination of crystal structures based on averaged local bond order parameters. *J. Chem. Phys.* **129**, 114707 (2008).
59. Kresse, G. & Furthmüller, J. Efficiency of ab-initio total energy calculations for metals and semiconductors using a plane-wave basis set. *Comput. Mater. Sci.* **6**, 15–50 (1996).
60. Kresse, G. & Furthmüller, J. Efficient iterative schemes for ab initio total-energy calculations using a plane-wave basis set. *Phys. Rev. B* **54**, 11169–11186 (1996).
61. Kresse, G. & Hafner, J. Ab initio molecular dynamics for liquid metals. *Phys. Rev. B* **47**, 558–561 (1993).
62. Perdew, J. P., Burke, K. & Ernzerhof, M. Generalized gradient approximation made simple. *Phys. Rev. Lett.* **77**, 3865–3868 (1996).
63. Hoover, W. G. Canonical dynamics: equilibrium phase-space distributions. *Phys. Rev. A* **31**, 1695–1697 (1985).
64. Nosé, S. Constant temperature molecular dynamics methods. *Prog. Theor. Phys. Suppl.* **103**, 1–46 (1991).

65. Thompson, A. P. et al. LAMMPS: a flexible simulation tool for particle-based materials modelling at the atomic, meso and continuum scales. *Comput. Phys. Commun.* **271**, 108171 (2022).
66. Kim, J.-S. et al. Second nearest-neighbour modified embedded-atom method interatomic potentials for the Pt–M (M = Al, Co, Cu, Mo, Ni, Ti, V) binary systems. *Calphad* **59**, 131–141 (2017).
67. Jeong, G.-U., Park, C. S., Do, H.-S., Park, S.-M. & Lee, B.-J. Second nearest-neighbour modified embedded-atom method interatomic potentials for the Pd–M (M = Al, Co, Cu, Fe, Mo, Ni, Ti) binary systems. *Calphad* **62**, 172–186 (2018).
68. Mendelev, M. I. *Ni–Co–Cr Interatomic Potential (EAM/FS)*. Interatomic Potentials Repository (National Institute of Standards and Technology, 2024).
69. Larsen, P. M., Schmidt, S. & Schiøtz, J. Robust structural identification via polyhedral template matching. *Model. Simul. Mater. Sci. Eng.* **24**, 055007 (2016).
70. Stukowski, A. Visualization and analysis of atomistic simulation data with OVITO: the Open Visualization Tool. *Model. Simul. Mater. Sci. Eng.* **18**, 015012 (2010).
71. de Fontaine, D. The number of independent pair-correlation functions in multicomponent systems. *J. Appl. Crystallogr.* **4**, 15–19 (1971).
72. Brandon, D. G. The structure of high-angle grain boundaries. *Acta Metall.* **14**, 1479–1484 (1966).

Acknowledgements

This work was primarily supported by the US Department of Energy, Office of Science, Basic Energy Sciences, Division of Materials Sciences and Engineering, under award number DE-SC0010378. The ADF-STEM imaging with TEAM 0.5 was performed at the Molecular Foundry, which is supported by the US Department of Energy, Office of Science, Office of Basic Energy Sciences, under contract number DE-AC02-05CH11231.

Author contributions

J.M. conceived of and directed the project. J.Z., P.E. and J.M. discussed and/or carried out the AET experiments. Y. Yuan, Yao Yang, S.M. and J.M. performed the image reconstruction, atom tracing and classification for the AET experiments. Y. Yuan, S.M. and J.M. analysed the data and interpreted the results. J.M., A.Y., D.S.K., Y. Yuan and Yongsoo Yang developed the GNP. C.L. and W.C. performed the AIMD simulations. K.L. and Q.A. conducted the MD simulations. J.M., Y. Yuan and S.M. wrote the paper. All authors commented on the paper.

Competing interests

The authors declare no competing interests.

Additional information

Extended data is available for this paper at https://doi.org/10.1038/s41563-026-02727-y.

Correspondence and requests for materials should be addressed to Jianwei Miao.

https://doi.org/10.1038/s41563-026-02727-y

Extended Data Table 1 | AET data collection, processing, reconstruction, refinement, and statistics of the 25 HEA nanoparticles

	HEA1	HEA2	HEA3	HEA4	HEA5	HEA6	HEA7	HEA8	HEA9	HEA10
Data collection and processing										
Voltage (kV)	200	200	200	200	200	200	200	200	200	200
Convergence semi-angle (mrad)	25	25	25	25	25	25	25	25	25	25
Probe size (Å)	0.8	0.8	0.8	0.8	0.8	0.8	0.8	0.8	0.8	0.8
Detector inner angle (mrad)	38	38	38	38	38	38	38	38	38	38
Detector outer angle (mrad)	190	190	190	190	190	190	190	190	190	190
Depth of focus (nm)	8	8	8	8	8	8	8	8	8	8
Pixel size (Å)	0.347	0.347	0.347	0.347	0.347	0.347	0.347	0.347	0.347	0.347
# of images	55	54	50	51	52	46	54	54	55	54
# of frames/angle	4	4	3	3	3	3	3	3	4	3
Tilt range (°)	-69.4	-74.7	-65.1	-69.3	-67.1	-58.7	-71.7	-72.5	-69.2	-67.9
	+72.6	+63.6	+71.5	+63.4	+69.2	+74.9	+69.4	+63.4	+72.1	+70.7
Total electron dose (10^5 e^- $Å^{-2}$)	9.5	9.3	7.0	7.1	7.3	6.4	7.6	7.6	10.2	7.5
Reconstruction										
Algorithm	RESIRE	RESIRE	RESIRE	RESIRE	RESIRE	RESIRE	RESIRE	RESIRE	RESIRE	RESIRE
Oversampling ratio	4	4	4	4	4	4	4	4	4	4
Number of iterations	200	200	200	200	200	200	200	200	200	200
Refinement										
R_1 (%)[a]	9.54	9.97	9.87	12.32	10.69	9.58	10.90	11.57	7.44	8.49
R (%)[b]	6.45	5.84	7.06	9.87	7.76	6.41	7.68	8.98	4.12	6.26
B′ factors ($Å^2$)										
Type 1	48.9	53.0	56.7	55.4	55.2	55.7	44.0	48.4	47.1	43.0
Type 2	46.4	54.6	56.6	47.3	46.3	54.4	44.0	44.3	53.8	49.7
Type 3	52.3	59.9	54.0	37.4	43.0	57.0	40.9	39.6	38.1	38.4
Statistics										
# of atoms										
Total	18356	18483	4640	2063	9755	11055	4661	3447	31235	8065
Type 1	8322	7467	1339	648	3901	4206	1079	1116	8017	1962
Type 2	6896	6936	1865	937	4213	4490	1906	1327	13389	3180
Type 3	3138	4080	1436	478	1641	2359	1676	1004	9829	2923

	HEA11	HEA12	HEA13	HEA14	HEA15	HEA16	HEA17	HEA18	HEA19	HEA20
Data collection and processing										
Voltage (kV)	300	200	200	200	300	200	200	200	200	200
Convergence semi-angle (mrad)	17	25	25	25	17	25	25	25	25	25
Probe size (Å)	0.7	0.8	0.8	0.8	0.7	0.8	0.8	0.8	0.8	0.8
Detector inner angle (mrad)	30	38	38	38	30	38	38	38	38	38
Detector outer angle (mrad)	195	190	190	190	195	190	190	190	190	190
Depth of focus (nm)	14	8	8	8	14	8	8	8	8	8
Pixel size (Å)	0.469	0.347	0.347	0.347	0.469	0.347	0.347	0.347	0.347	0.347
# of images	52	52	54	56	53	51	53	51	53	59
# of frames/angle	4	3	3	3	3	3	3	4	3	3
Tilt range (°)	-72.6	-70.3	-69.6	-69.6	-72.6	-69.1	-69.6	-69.3	-71.7	-66.6
	+67.4	+66.3	+74.0	+71.8	+66.4	+64.7	+74.0	+63.4	+69.4	+78.0
Total electron dose (10^5 e^- $Å^{-2}$)	3.4	7.2	7.6	7.8	3.5	7.1	7.4	9.5	7.4	8.2
Reconstruction										
Algorithm	RESIRE	RESIRE	RESIRE	RESIRE	RESIRE	RESIRE	RESIRE	RESIRE	RESIRE	RESIRE

https://doi.org/10.1038/s41563-026-02727-y

Extended Data Table 1 (continued) | AET data collection, processing, reconstruction, refinement, and statistics of the 25 HEA nanoparticles

	HEA11	HEA12	HEA13	HEA14	HEA15	HEA16	HEA17	HEA18	HEA19	HEA20
Oversampling ratio	4	4	4	4	4	4	4	4	4	4
Number of iterations	200	200	200	200	200	200	200	200	200	200
Refinement										
R_1 (%)[a]	7.43	13.02	8.46	7.61	6.81	11.79	9.38	9.95	7.62	6.10
R (%)[b]	4.39	11.19	5.89	5.10	3.95	8.77	7.46	6.48	5.66	3.16
B′ factors (Å^2)										
Type 1	33.9	33.7	45.8	53.8	42.1	31.0	35.5	33.9	55.6	51.8
Type 2	35.1	32.5	46.4	56.4	44.2	31.1	34.5	32.8	58.0	50.4
Type 3	31.6	33.9	40.9	39.1	36.0	30.7	34.6	29.9	42.1	45.2
Statistics										
# of atoms										
Total	101881	11223	10053	12245	72680	12244	7739	3696	6648	28916
Type 1	23644	4737	2638	2547	15748	5055	2158	872	1579	5846
Type 2	46432	4206	3830	5264	32908	4639	2750	1735	2430	12227
Type 3	31805	2280	3585	4434	24024	2550	2831	1089	2639	10843

	HEA21	HEA22	HEA23	HEA24	HEA25
Data collection and processing					
Voltage (kV)	200	200	200	200	200
Convergence semi-angle (mrad)	25	25	25	25	25
Probe size (Å)	0.8	0.8	0.8	0.8	0.8
Detector inner angle (mrad)	38	38	38	38	38
Detector outer angle (mrad)	190	190	190	190	190
Depth of focus (nm)	8	8	8	8	8
Pixel size (Å)	0.347	0.347	0.347	0.347	0.347
# of images	53	56	56	53	52
# of frames/angle	4	3	3	3	3
Tilt range (°)	-65.8	-66.6	-72.0	-71.0	-70.1
	+72.5	+75.8	+72.0	+73.0	+66.1
Total electron dose (10^5 e^- Å^{-2})	9.8	7.8	7.8	7.4	7.2
Reconstruction					
Algorithm	RESIRE	RESIRE	RESIRE	RESIRE	RESIRE
Oversampling ratio	4	4	4	4	4
Number of iterations	200	200	200	200	200
Refinement					
R_1 (%)[a]	6.44	7.90	8.21	7.07	12.39
R (%)[b]	4.61	5.60	5.84	5.35	10.28
B′ factors (Å^2)					
Type 1	38.1	41.6	35.5	40.9	24.6
Type 2	37.9	37.6	34.5	39.5	25.5
Type 3	36.1	36.3	34.6	39.8	29.2
Statistics					
# of atoms					
Total	21177	5672	6037	10232	4292
Type 1	4865	1124	1446	3138	1903
Type 2	8861	2356	2045	3898	1431
Type 3	7451	2192	2546	3196	958

[a]The R_1-factor is defined as Eq. (5) in ref. 56. [b]The R-factor is defined in Eq. (4) in ref. 43.

https://doi.org/10.1038/s41563-026-02727-y

Extended Data Table 2 | Parameters for fitting experimentally measured BOO data to a generalized Gaussian distribution function

	Nuclei size*	α_0	R (Å)	β
HEA	1–10	0.63	9.78	1.27
	11–100	0.79	13.13	1.29
	101–500	0.89	14.91	1.33
	501–1000	0.96	14.63	1.64
	>1000	0.98	13.46	2.66
MEA	1–10	0.73	12.64	1.19
	11–100	0.87	14.72	1.22
	101–200	0.93	14.17	1.40
	201–300	0.96	13.86	1.81
	>300	0.98	13.79	2.20

*Nucleus size denotes the number of atoms with BOO ≥ 0.5 in each nucleus.

https://doi.org/10.1038/s41563-026-02727-y

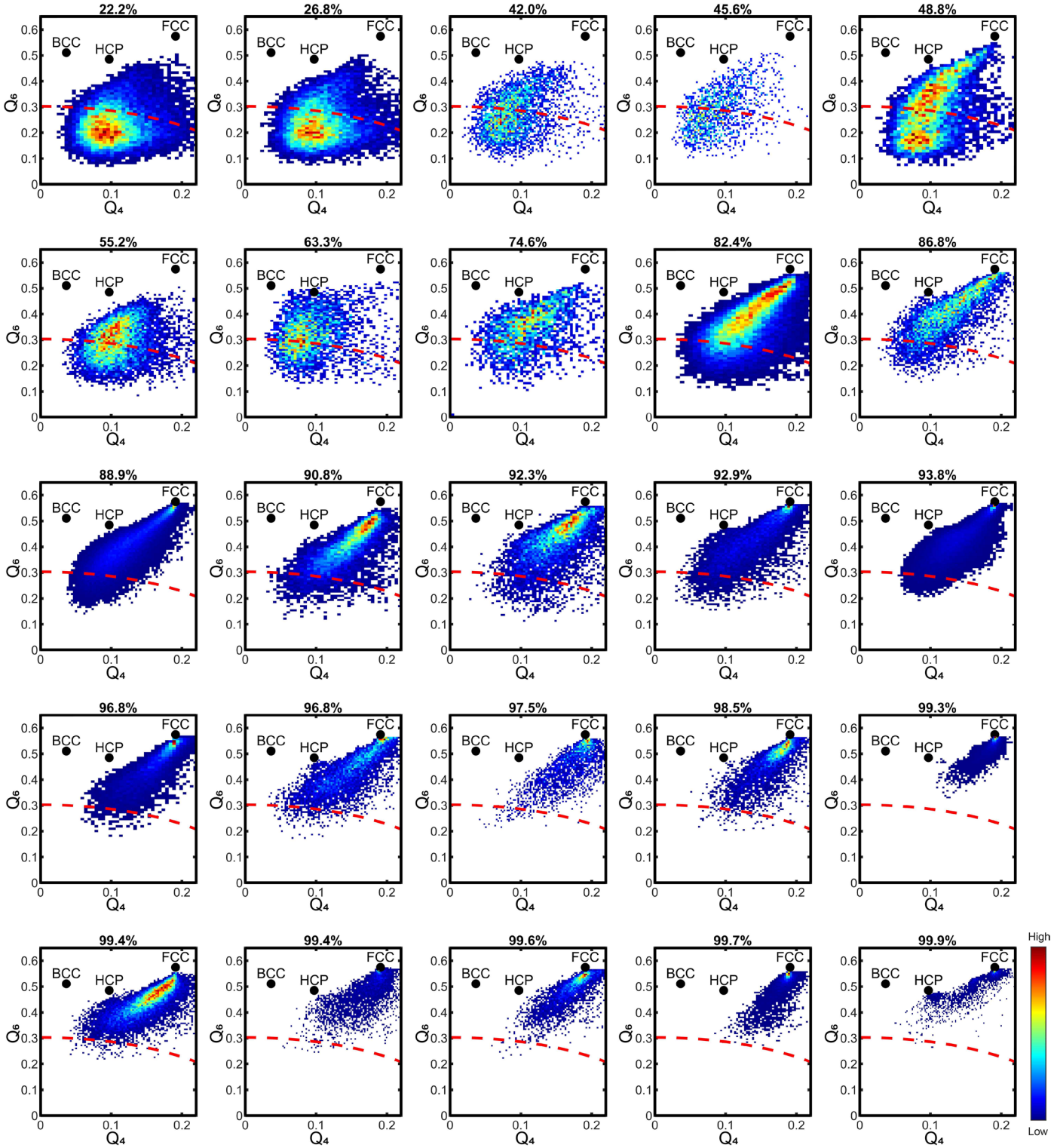

Extended Data Fig. 1 | Q_4-Q_6 bond-order distributions for HEA1-HEA25. The black dots indicate ideal bcc, hcp and fcc reference values. The degree of crystallinity, defined as the percentage of atoms in each nanoparticle with BOO ≥ 0.5, increases from 22.2% in HEA1 to 99.9% in HEA25. The red dashed curves mark normalized BOO = 0.5.

https://doi.org/10.1038/s41563-026-02727-y

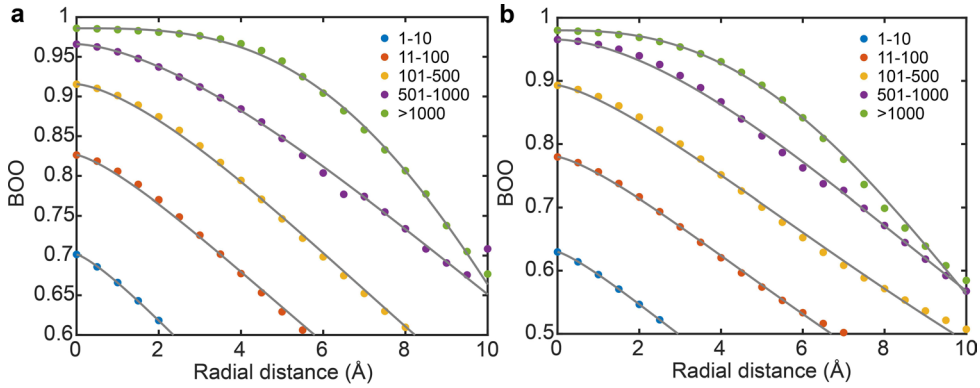

Extended Data Fig. 2 | Robustness of BOO analysis to threshold choice and experimental uncertainty. a, Average BOO profiles as a function of radial distance for five nucleus size groups, computed with a stricter BOO cutoff of 0.6 for nucleus identification. Solid curves are generalized Gaussian fits. **b**, Same analysis after propagating experimental 3D positional uncertainty by adding random displacements consistent with the measured positional precision (RMSD = 21 pm) to all atomic coordinates and repeating the full analysis with a BOO cutoff of 0.5. The resulting profiles for the same five size groups remain consistent with the unperturbed data (Fig. 3c).

https://doi.org/10.1038/s41563-026-02727-y

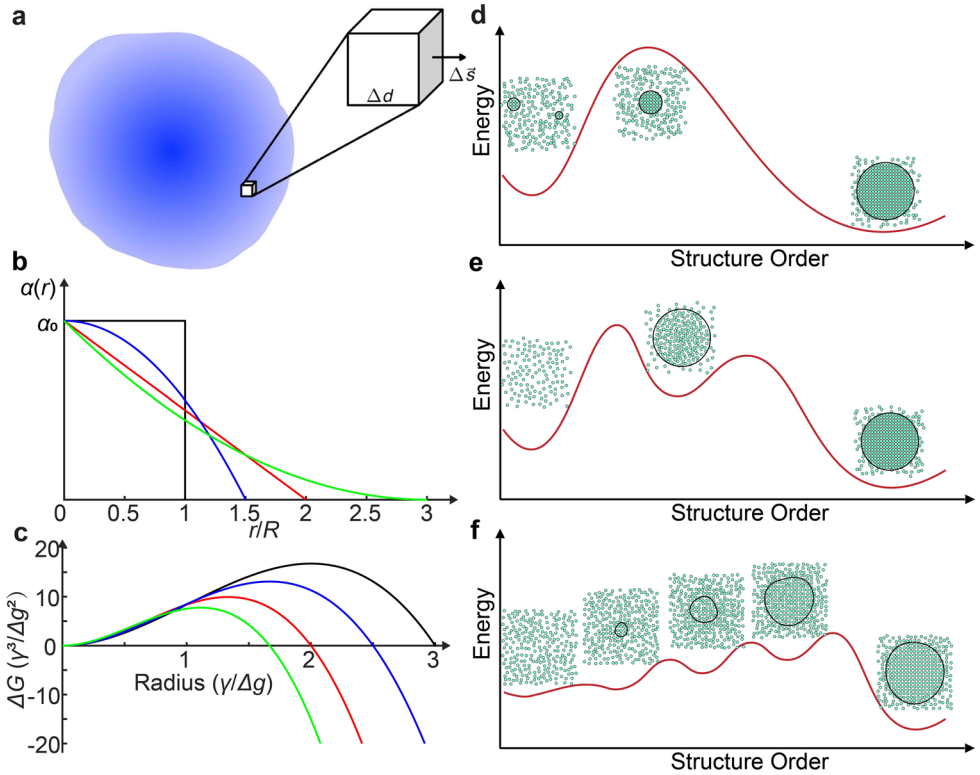

Extended Data Fig. 3 | Comparison of CNT, the two-step model, and GNP. **a**, In GNP, a schematic nucleus is partitioned into small interfacial elements with surface area Δs and thickness Δd, which are used to evaluate the interfacial term in Eq. (1). **b**, Four illustrative radial order-parameter profiles, $\alpha(r)$: a Heaviside step (black; CNT limit), a linear ramp (red), and two parabolic profiles (blue and green); α_0 denotes the core value of the order parameter. **c**, Total free energy change ΔG computed with Eq. 1 for the profiles in (**b**). As the profiles become progressively less diffuse and approach the sharp-interface limit (green, red, blue and black), the nucleation free-energy barrier increases, with the step profile yielding the highest barrier and recovering CNT. **d**–**f**, Schematic free-energy landscapes for CNT (**d**), the two-step model (**e**), and GNP (**f**). CNT exhibits a single barrier; the two-step model includes a metastable precursor minimum and a second barrier; GNP proceeds through multiple evolving intermediate states with a gradually increasing barrier.

https://doi.org/10.1038/s41563-026-02727-y

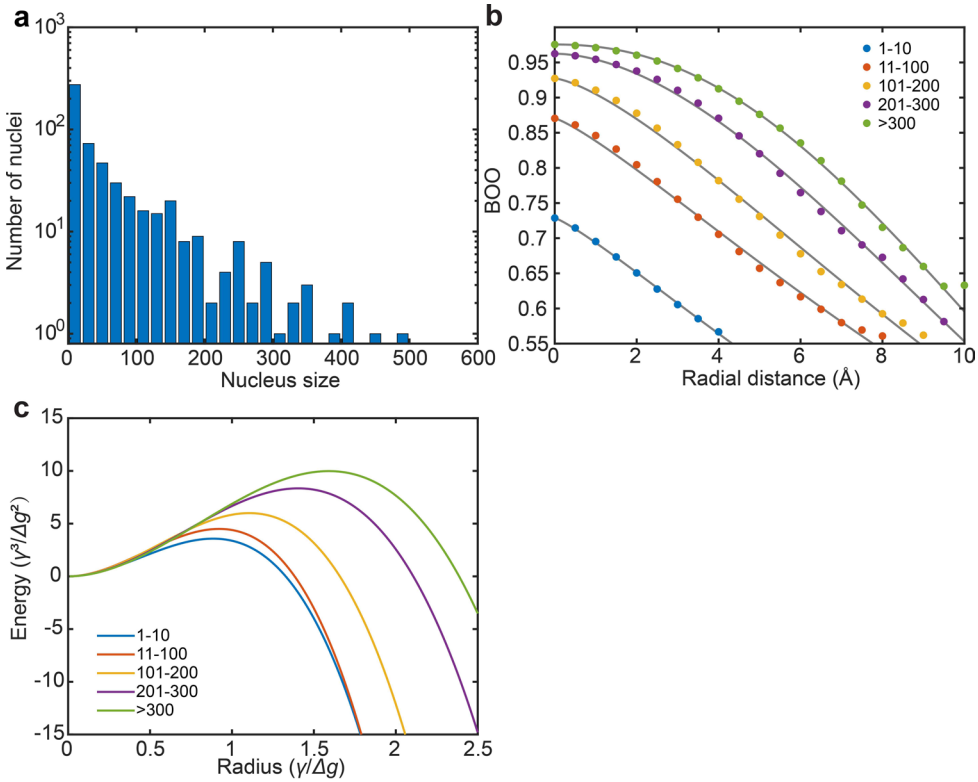

Extended Data Fig. 4 | Analysis of 498 nuclei from six NiPdPt MEA nanoparticles. a, Exponential decrease in the number of nuclei as their size increases. **b**, Average BOO profiles as a function of radial distance for five nucleus-size classes: 1-10 (blue dots), 11-100 (red dots), 101-200 (yellow dots), 201-300 (purple dots), and >300 (green dots). The solid curves represent fits to a generalized Gaussian distribution function. **c**, Total free energy change as a function of radial distance, calculated by substituting the experimentally fitted BOO profiles in (b) for $\alpha(r)$ in Eq. (1), showing that the nucleation free-energy barrier increases as the ordered region expands.

https://doi.org/10.1038/s41563-026-02727-y

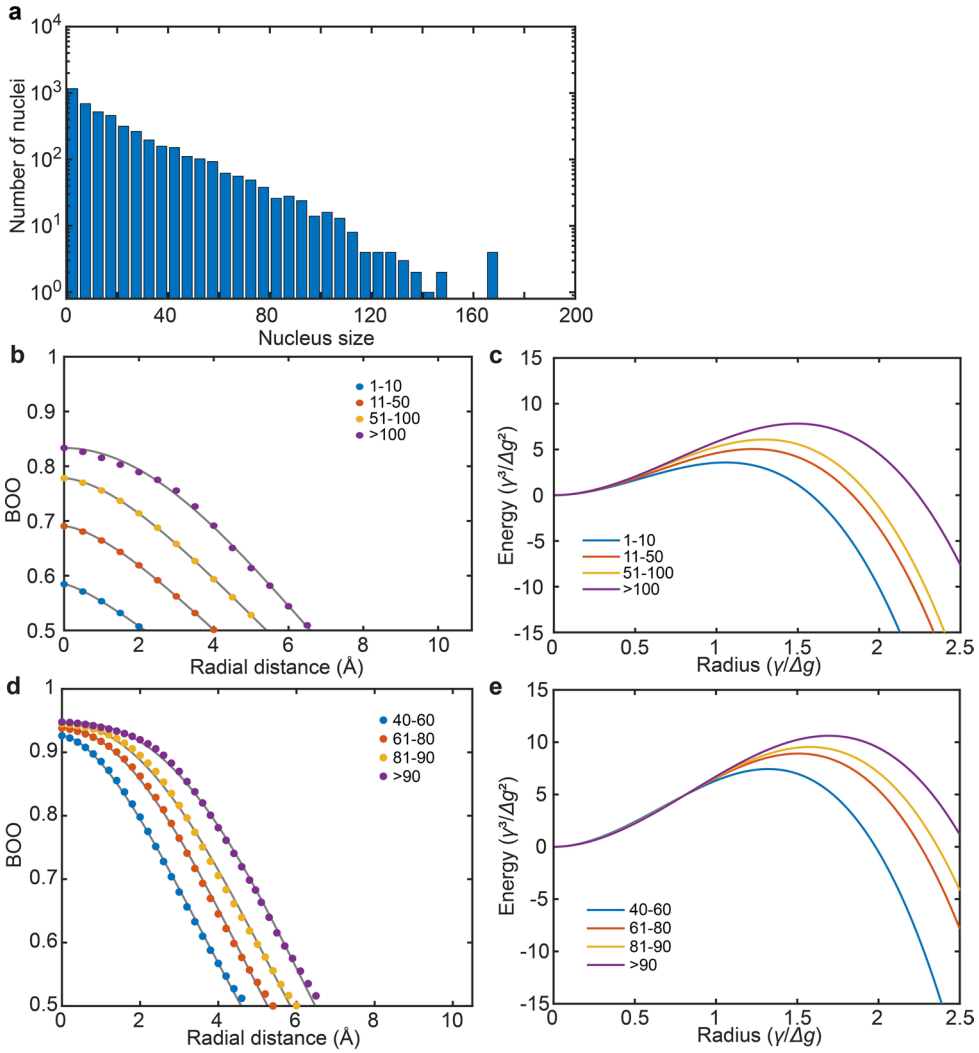

Extended Data Fig. 5 | AIMD simulations capturing the process of crystal nucleation in HEAs during cooling from 2,300 K to 300 K. a, An exponential decrease in the number of nuclei is observed as a function of their size. **b**, Average BOO profiles as a function of radial distance for four nucleus-size classes. Solid curves are generalized Gaussian fits. **c**, Total free energy change as a function of radial distance, calculated by substituting the fitted AIMD-simulated BOO profiles in (**b**) for $\alpha(r)$ in Eq. (1). **d**, BOO profiles as a function of radial distance, tracking the growth of a single nucleus during cooling from 1,300 K to 700 K. **e**, Total free energy variation as a function of radial distance from the nucleus, calculated by substituting the fitted AIMD-simulated BOO profiles in (**d**) for $\alpha(r)$ in Eq. (1).

https://doi.org/10.1038/s41563-026-02727-y

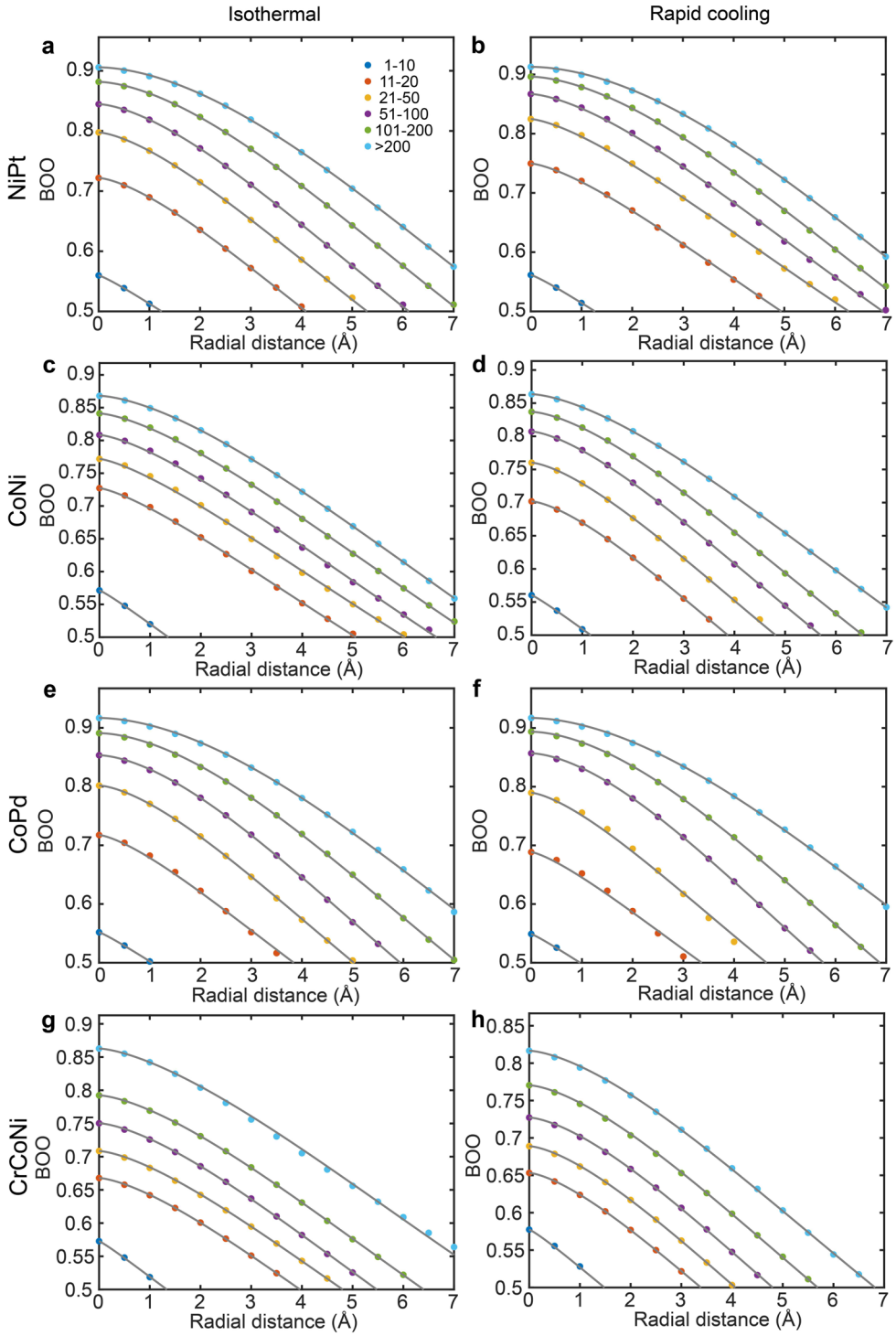

Extended Data Fig. 6 | BOO profiles from MD simulations under isothermal and rapid-cooling conditions. a-h, Average BOO profiles as a function of radial distance for six nucleus size groups. Simulations were performed for binary alloys NiPt (**a**, **b**), CoNi (**c**, **d**), CoPd (**e**, **f**), and the ternary alloy CrCoNi (**g**, **h**). Isothermal nucleation was modelled by cooling the liquid to and holding it at a fixed supercooled temperature, whereas rapid-cooling nucleation was modelled with a cooling rate of 1×10^{10} K s^{-1}. Solid curves are fits to a generalized Gaussian distribution. These results show that the gradual BOO variation from core to boundary is an intrinsic feature of nucleation and is robust across cooling conditions.

https://doi.org/10.1038/s41563-026-02727-y

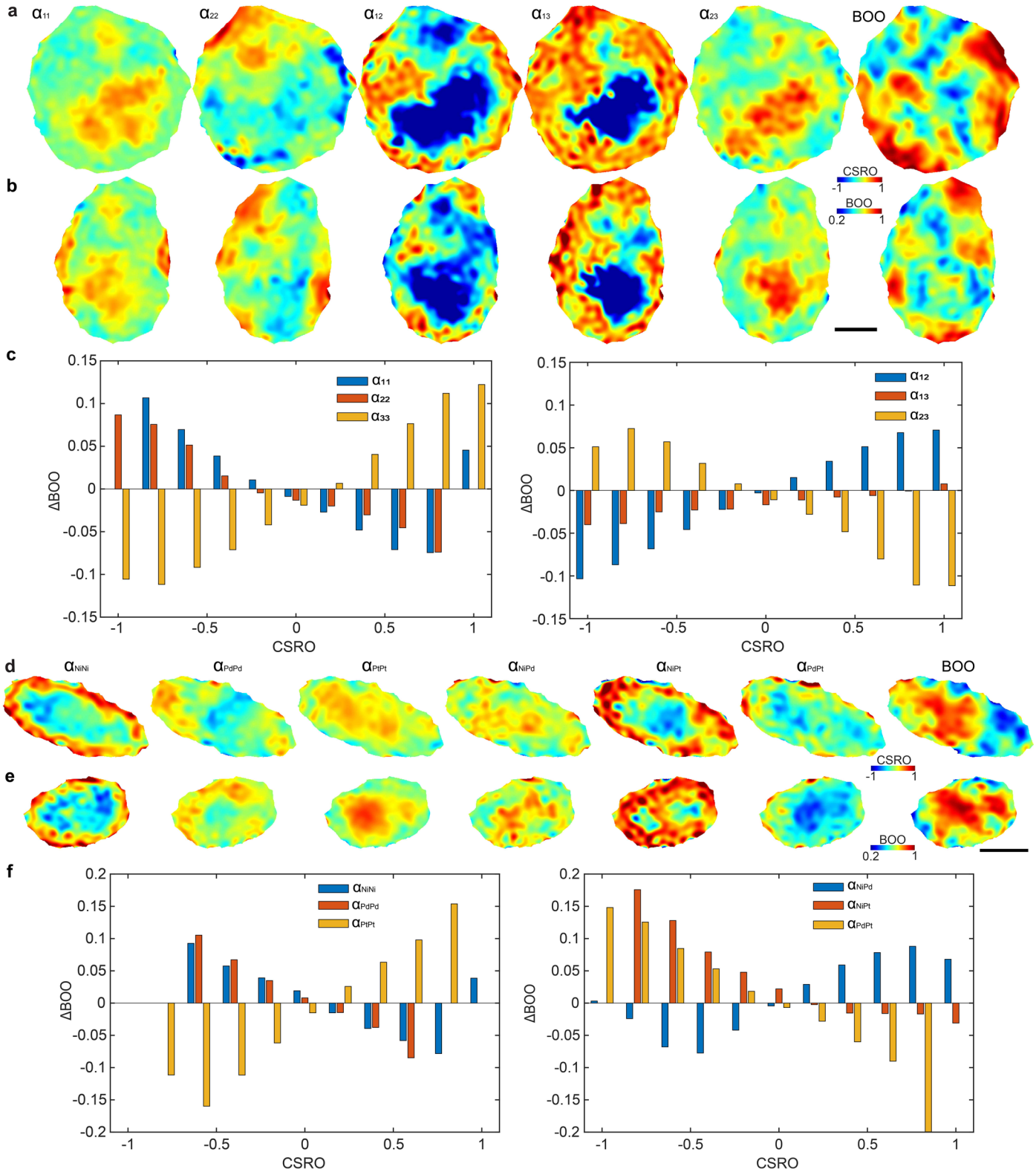

Extended Data Fig. 7 | Coupling between local structural and chemical order in HEAs and MEAs. a, **b**, XY and XZ slices from HEA10 showing spatial maps of five CSRO parameters (α_{11}, α_{22}, α_{12}, α_{13}, α_{23}) together with the BOO field; the remaining parameter α_{33} is shown in Fig. 4. **c**, Change in BOO, ΔBOO, versus each CSRO parameter, averaged over 25 HEA nanoparticles. **d**, **e**, XY and XZ slices from a representative NiPdPt MEA nanoparticle, with Ni, Pd, and Pt resolved individually, showing spatial maps of six CSRO parameters (α_{NiNi}, α_{PdPd}, α_{PtPt}, α_{NiPd}, α_{NiPt}, α_{PdPt}) and BOO. **f**, Change in BOO, ΔBOO, versus each CSRO parameter, averaged over six MEA nanoparticles. Scale bars, 2 nm.

https://doi.org/10.1038/s41563-026-02727-y

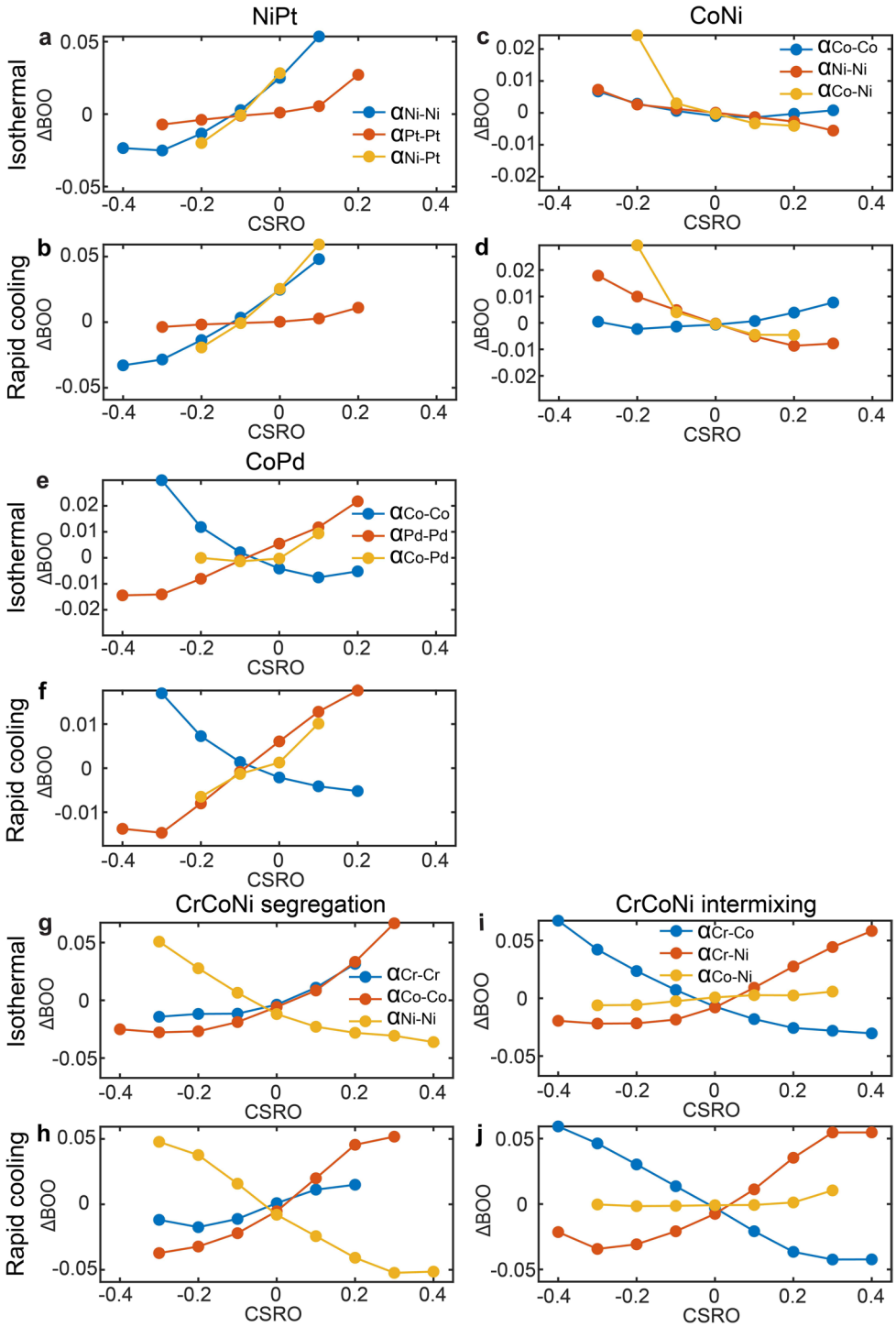

Extended Data Fig. 8 | Correlation between local chemical order and structural ordering in MD simulations across alloy compositions. a-j, Change in BOO, ΔBOO, plotted against CSRO parameters for NiPt (**a**, **b**), CoNi (**c**, **d**), CoPd (**e**, **f**), and CrCoNi (**g**-**j**). Two nucleation protocols were employed: isothermal nucleation at fixed supercooling and continuous quenching at 1×10^{10} K s^{-1}. Nuclei were identified using the same BOO ≥ 0.5 criterion as in the experiments to enable direct comparison. Across alloys and protocols, ΔBOO varies systematically with CSRO, indicating that chemistry–structure coupling during nucleation is composition dependent yet robust across cooling conditions.